

NANOSCINTILLATORS FOR RADIATION DETECTION

by

RYAN GREGORY HALL

Presented to the Faculty of the Graduate School of  
The University of Texas at Arlington in Partial Fulfillment  
of the Requirements  
for the Degree of

MASTER OF SCIENCE IN PHYSICS

THE UNIVERSITY OF TEXAS AT ARLINGTON

May 2013

Copyright © by Ryan Gregory Hall 2013

All Rights Reserved



## Acknowledgements

First and foremost, my thanks go to Dr. Chen both for his support and guidance, and for ensuring that I am always learning new concepts and new techniques. Without his efforts, I would likely have never gotten past my first solid-state synthesis so many months ago. My committee—Drs. Brandt, Kenarangui, and Weiss—also deserve my gratitude, for each of them guided my growth as a scientist in his own way. The lessons that they taught me are critical components that I hope to keep with me for the rest of my career, in science and beyond. And while the final defense presentation was a solo effort, there are so many who contributed to reaching that stage: Mingzhen Yao for first getting me started, Jiang Ke, Marius Hossu, and Lun Ma for answering my questions even in the midst of their own research conundrums, and my labmates present and emeritus, Homa, Brian, Sunil, Leila, and Tej, for their encouraging words and enlightening discussions on topics of every sort. For the Physics staff, Margie, Bethany, Stacey, and Robin, for their valiant efforts to keep us absent-minded scientist types in the good graces of the wider administration, well-equipped for research and the presentation thereof, and off the Customs naughty list; and for Jimmy Hanhart and the late Howard Bailiff for turning the messy sketches of an inexperienced grad into devices for precision measurement.

Finally, my thanks go to my present and future family for their encouragement. To my parents: thank you a thousand times for fostering my curiosity through whatever paths it led me down, and for making sure that I spelled “entomologist” correctly and pushing me towards PBS instead of Power Rangers. To my sister Beate, thanks for talking science and watching Nova, and inspiring so many with your baked goods and cheerful attitude—I wish you the best in your future work, as well.

And last, but of no little importance, thank you to my lovely Cassandra, for putting up with my writing all the time, for helping me be presentable for conferences and other reports, and for everything else you do to make me more awesome.

22 April 2013

Abstract

NANOSCINTILLATORS FOR RADIATION DETECTION

Ryan Hall, M.S.

The University of Texas at Arlington, 2013

Supervising Professor: Wei Chen

In the search for faster, more effective methods for detection of and protection against radiological weapons, advances in materials for radiation detection are a critical component of any successful strategy. This work focuses on producing inexpensive, but highly sensitive, nanoparticle alternatives to existing single-crystal installations. Attention is given to particular types of promising inorganic scintillators:  $\text{LaF}_3$ , yttrium-aluminum-garnet (YAG), and  $\text{SrF}_2$ , each one an inorganic host doped with additional elements that encourage luminescent decay and increase effective Z-value. I examine the possible routes to synthesize these compounds, and the difficulties and benefits of each method. After synthesizing these materials, testing was performed to determine comparative performance against each other and commercial solutions, identify structural and compositional characteristics, and explore routes for fixing the scintillators into a detector assembly. The unifying goal is to develop a scintillating material suitable for consistent dosimetry and radio-isotope identification applications.

## Table of Contents

Acknowledgements .....	iii
Abstract .....	iv
List of Illustrations .....	vii
List of Tables .....	viii
Chapter 1 Introduction.....	1
Chapter 2 Background and Motivation.....	4
2.1 Scintillating Materials .....	4
2.1.1 Plastic Scintillators and Dyes .....	7
2.1.2 Liquid Scintillators.....	8
2.1.3 Quantum Dots .....	9
2.1.4 Commercial Single-Crystals.....	9
2.1.5 Comparison with Nanoparticle Scintillator Materials .....	10
2.2 Operating Principles of Radiation Detectors .....	11
2.2.1 Geiger-Müller Tubes .....	12
2.2.2 Proportional Counters .....	13
2.2.3 Semiconductor-based Detectors .....	13
2.2.4 Scintillation Counters .....	14
2.3 Energy Transfer Techniques.....	15
2.3.1 Luminescent Energy Transfer .....	16
2.3.2 Förster Resonance Energy Transfer .....	17
Chapter 3 Materials and Synthesis Procedures.....	19
3.1 Lanthanum Fluoride .....	19
3.1.1 Solid State Diffusion .....	19
3.1.2 Wet Chemistry .....	20
3.2 Yttrium Aluminum Garnet .....	21
3.2.1 Solid State Diffusion and Combustion Methods .....	21

3.2.2 Microwave Synthesis .....	22
3.2.3 Modified Glycothermal Technique .....	23
3.2.4 Coprecipitation Method.....	24
3.3 Strontium Fluoride .....	24
3.3.1 Solid-State Diffusion.....	25
3.4 Commercial Comparison: NaI(Tl).....	26
Chapter 4 Testing and Results .....	29
4.1 Characterization Techniques .....	29
4.1.1 Photoluminescence Appraisal .....	29
4.1.2 X-ray Excited Luminescence .....	31
4.1.3 Gamma Ray Stimulation and Scintillation Counting .....	33
4.1.4 X-ray Diffraction.....	35
4.2 Synthesized Material Analysis .....	35
4.2.1 Sodium Iodide (Thallium Activated).....	36
4.2.2 Lanthanum Fluoride .....	36
4.2.3 Yttrium Aluminum Garnet .....	40
4.2.4 Strontium Fluoride .....	43
Chapter 5 Conclusions and Extension to Future Research .....	49
5.1 Evaluation of Nanoparticle Performance .....	49
5.2 Project Extension.....	51
Appendix A Apparatus and Instrumentation .....	53
References .....	57
Biographical Information .....	59

## List of Illustrations

Figure 2.1: Diagram of the scintillation process. ....	5
Figure 2.2: Bicron NaI(Tl) commercial scintillator. ....	10
Figure 3.1: PL and XL of a commercial NaI(Tl) scintillator. ....	27
Figure 3.2: Gamma scintillation response of NaI(Tl) crystal. ....	28
Figure 3.3: Integrated counts for NaI(Tl). ....	28
Figure 4.1: Sample photoluminescence and x-ray luminescence spectra. ....	30
Figure 4.2: YAG:Ce demonstrating Stokes shift. ....	31
Figure 4.3: Photo and schematic of $\gamma$ scintillation test station. ....	33
Figure 4.4: Selected PL spectra of $\text{LaF}_3\text{:Ce,Tb}$ . ....	37
Figure 4.5: Selected XL spectra of $\text{LaF}_3\text{:Ce,Tb}$ . ....	38
Figure 4.6: XL emissions of $\text{LaF}_3\text{:Ce}$ prepared through EtOH / oleic acid wet synthesis. ....	39
Figure 4.7: XRD analysis of YAG:Ce nanoparticles. ....	41
Figure 4.8: PL and XL results of YAG:Ce samples. ....	42
Figure 4.9: XL emissions of YAG:Ce,Yb samples. ....	42
Figure 4.10: PL response of $\text{CaF}_2$ and $\text{SrF}_2$ produced through various conditions. ....	43
Figure 4.11: Two-peak emission from $\text{SrF}_2\text{:Mn,Eu}$ . ....	43
Figure 4.12: Initial x-ray response from $\text{SrF}_2$ samples. ....	44
Figure 4.13: 90 kV x-ray response over time in $\text{SrF}_2\text{:Mn,Eu} \cdot \text{v3}$ . ....	44
Figure 4.14: 50 kV x-ray testing of $\text{SrF}_2\text{:Mn,Eu}$ . ....	46
Figure 4.15: $\text{SrF}_2\text{:Mn,Eu}$ gamma scintillation response. ....	48
Figure 5.1: FIR and $\gamma$ luminescence testing assembly. ....	52
Figure A.1: Interior and exterior of x-ray irradiation system. ....	55
Figure A.2: Interior of Shimadzu spectrofluorophotometer. ....	56
Figure A.3: OceanOptics spectrometer. ....	56

## List of Tables

Table 3.1: Synthesis conditions of selected $\text{SrF}_2$ , $\text{MgF}_2$ , and $\text{CaF}_2$ samples.....	26
---	----



## Chapter 1

### Introduction

On December 2, 1942, mankind initiated the first controlled release of nuclear energy through fission. The team of scientists responsible for this feat, led by Enrico Fermi and standing on the shoulders of giants like Rutherford and the Curies, ushered in a new era of power, politics, and popular misunderstanding. The growth and spread of nuclear energy, both fission and fusion, controlled and uncontrolled, continues to hold a place as one of the most controversial and misunderstood aspects of physics – at least among non-technical audiences. Despite some notable incidents, such as the cluster of events surrounding Fukushima, commercial nuclear power generation has maintained an impressive safety record, with only a handful of accidents in over 14,000 reactor-years of operation[1,2]. The organizations who construct and operate these facilities purposely design in robustness; reactors are built to minimize the chance of a catastrophic event, and, if all safeties fail and the worst case scenario occurs, to minimize the human impact. Outside of fission power production, the situation becomes more complicated. What happens when interested parties actively seek increased purification of uranium? When the 5%  $^{235}\text{U}$  necessary for fuel rods is no longer sufficient?

In the last decade, the threat of nuclear proliferation and eventual possession of devices by non-rational actors, rogue states, and terrorist groups has increased the need for systems to defend against these types of threats. A radioactive dispersal device (RDD—a dirty bomb) has severe implications for the long term health of those it affects, and the target could be anywhere that people congregate. Searching for signs of these devices presents additional difficulties: if a low-activity or shielded radioisotope is used, it may be difficult to spot that signal over background measurements. With current technologies, that level of sensitivity often dictates an invasive secondary search, sometimes triggered by common materials like concrete mix or by the residue of medical isotope treatments. The situation as a whole presents a conflict between guaranteeing the safety of the people from a radioactive threat and the preservation of the civil liberties and convenience that have become the ideal in the United States. It is the search for balance

between these two views, each accompanied by a phalanx of secondary visions, which encourages the development and application of new search and forensics technologies.

Though 2015 will most likely not bring omnipresent hovercars or a permanent lunar settlement, much of the high-tech innovation in the late 20<sup>th</sup> century would outshine the prognostication of early science fiction writers. Each new technology built on the principles and concepts of previous work, with that additional spark of a question, “How can we improve this system?” comes from innovators who broke from the herd. From biotech to energy storage, optics to computing, the compounded increase of knowledge leads to an endless array of novelties. In particular, in-depth studies of biological systems and the fantastic constructs developed deep within cells and diverse tissues has provided new inspiration for a variety of technologies. Researchers have produced artificial spider silk proteins from genetically modified *e. coli* bacteria[3]. Cancer patients have better prognoses due in part to the development of angiogenetic inhibitors – drugs which prevent the growth of blood vessels needed to sustain tumor cells[4]. Efforts in the macroscopic realm proceed apace, but the growing interest in the smaller components of nature, from quarks on up, continues to drive imaginative studies in new science. Just as in the eternal war between pathogens and the human immune system, though, the meter-scale arms race is heating up as well. Not always with new weapons, but with novel and destructive ways to cobble together simple RDDs. And, just as the enormous (from a cell’s viewpoint) human organism is protected by a complex system of microscopic agents, the human race can be protected by engineered particles at the nanoscale. One hot area in radiation detection research – please pardon the paronomism – is the design and construction of new materials and devices of dimensions less than 100 nanometers.

Nanotechnology incorporates a broad range of disciplines. For planning and design, knowledge of energy level structures and preferred bonding configurations is required from semiconductor and solid state physics. Chemistry and synthesis techniques are critical for producing the raw materials. At the final stages of a detector project, engineering and device design take center stage, as the luminescent material is configured for a portal monitoring system or handheld dosimetry device. Our work lies at a junction of these areas. The goal of the NanoBio Physics radiation detection division is to improve upon existing materials—bulk compounds or their nanoparticle analogs—or to produce entirely new reactive

nanocomposites to detect and identify radioactive sources. As with any technological exploration – well-established or cutting-edge – each step in further development necessitates re-evaluation of what once was considered unassailable fact. Nano-scintillators do not produce sufficient output to measure photopeaks? Solved[5]. Quantum dots have some useful emission properties, but no x-ray response. No longer an issue[6]. Need a cheap, sensitive detector to augment baggage and personnel scans? The material at hand discusses a possible class of scintillators to solve that issue as well.

The research undertaken in our lab seeks to demonstrate the efficacy of nanocompounds not just for radiation detection, but for treatments to fight cancer and other diseases as well. The same penetrative properties that make ionizing radiation so dangerous for uncontrolled exposure recommend it as an ideal candidate to non-invasively probe tumors and deep tissues. Radiation therapy has been in use since 1896, though certainly not in the laser-guided, fractionated modern sense. Even with modern techniques, this method of treatment can cause damage to surrounding healthy tissue in the quest to destroy a tumor. New nanoparticle technologies, some pioneered by the UTA NanoBio group and attendant collaborations, help to target radiation activity to a certain area, or reduce treatment side effects with lowered dose requirements[7].

Holistically, the NanoBio goal embodies an intent far beyond the facile production of literature or intellectual properties – though those are the easily-viewed signs of success. We intend to push the boundaries of technology designed to ensure security and health for all the people of the world. We have developed a strong partnership with UT Southwestern Medical Center to promote exploration of nanomedicine for cancer treatments, and have built connections with Pacific Northwest National Lab to work together towards optimal products. Currently, our group is seeking to join the UTA Research Institute to take the some of the concepts explored in our lab and bring them to market in affordable, cutting-edge solutions to the world's problems. It is through this sort of partnership, and other work in conjunction with national laboratories and interested commercial entities, that our research transitions from the abstract to the concrete.

## Chapter 2

### Background and Motivation

For this project, the primary focus was to examine materials which have demonstrated strong luminescence in either the nanoparticle or bulk form; following a preliminary evaluation, we will seek to replicate and improve bulk luminescent behavior at the nanoscale, or enhance nanoparticle luminescence to a level commensurate with the needs of radiation detection installations. Commercial scintillating materials such as single crystals of activated NaI or CsI produce a cascade of secondary, low-energy photons when excited by an incident x- or gamma ray. As shown in the diagram in Figure 2.1, an incoming  $\gamma$  excites an inner shell electron, completely ionizing it and leaving a positively-charged “hole” (left side of figure). Nearby electrons in higher-order shells then fall inward to fill the vacancy (center portion), leaving behind their own holes (dotted circles) and emitting excess energy through a secondary photon. In the last stage, the rearrangement of inner electrons has moved the hole into the valance shell, and the atom can then capture a free electron from the conduction band or one from an excited state in a nearby atom. This last stage produces the visible scintillation light that we seek to measure. This same process induces luminescence in nanoparticles, quantum dots, and plastics, among other components, but with some variation in the mechanism due to differing atomic numbers (effective  $Z$ ) and molecular energy levels available to electrons. For organic compounds which we will discuss later, like the dye 2,5-diphenyloxazole, the interactions occur at the molecular level, and the incoming  $\gamma$  ionizes electrons from the hybrid  $\pi$ -bonds which are a characteristic of many radio-sensitive organic compounds.

#### 2.1 Scintillating Materials

The core of any radiation detector contains some selection of materials responsive to the disruptive effects of ionizing radiation, and some system to measure the level of disruption. As we will discuss in section 2.2, the earliest counter designs used a gas mixture to take advantage of ionization processes, but lacked the extensible features requisite for advanced applications. Though some gas scintillators are used in detection of fission fragments or massive charged particles, the reaction mechanism of scintillating materials differs significantly from simple ionization. When an x- or gamma ray travels through a material, it can excite a variety of different electrons based on its energy. Absorption drops with photon energy as  $E^{-3}$

with peaks at each new affected electron shell up to  $\sim 100$  keV; photons above this range, typically in the gamma region, see a very small cross section. The shower of secondary photons emitted from an event is captured by a photomultiplier tube (PMT), which converts the optical measurement into a time-integrated electrical signal to determine the total amount of charge disturbed in the PMT. By considering the time-voltage area of each pulse, an electronics system can determine not only the presence of ionizing radiation, but can give a measurement of its energy. An extensive variety of compounds satisfies the condition of producing light when energetic radiation passes through, but few are useful at the performance levels needed in radiation detection and nuclear forensics. In fact, selection of detection material for a system of this type depends on several factors outside of basic scintillation qualities, including the following:

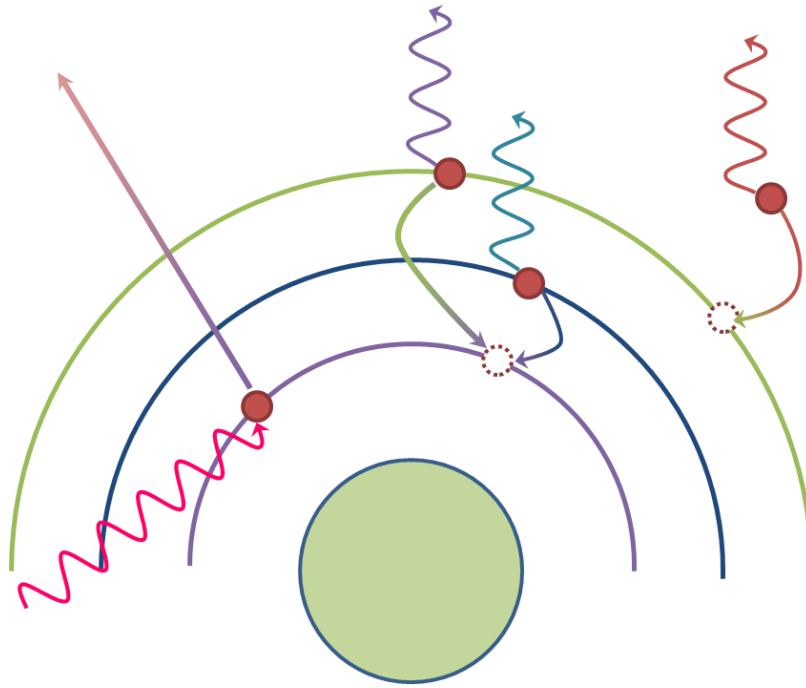


Figure 2.1: Diagram of the scintillation process.

An incoming  $\gamma$ -ray ionizes an inner-shell electron (left), creating a hole that is filled by outer electrons (center), which in turn leave behind their own holes. Finally, an electron from the conduction band fills the last vacancy, emitting a visible photon detected as scintillation luminescence (right).

Decay lifetime: the time required for emission intensity to drop from some 100% level to  $1/e$  of that quantity ( $\sim 37\%$ ), where  $e$  is Euler's number. Empirically, the decay time is a combination of multiple decay paths with different time constants, often referred to by "fast" and "slow" components. The mechanism underlying the disparity is described further in the sections discussing each material's properties. Faster decay times generally indicate better measurements, allowing separation of nearly-coincident events and less detector dead time between successfully registering events.

Linearity: a measure of the proportionality of detector response with incident energy. For scintillators, this is generally defined as some number of photons per keV deposited. For composite materials, additional effects like re-absorption or internal losses must be considered as modifiers to this value. Poor linearity affects the precision of spectroscopic measurements, limiting detector operations to some particular region where the scintillator response is still proportional.

Wavelength matching: the ability to tune the secondary photon output to the most sensitive (or lowest) noise regions of the accompanying PMT. We can tune quantum dot scintillators by adjusting their size; smaller particles emit shorter wavelengths. Other materials require secondary scintillators; these compounds work through energy transfer processes, detailed in section 2.3, to shift the final emitted wavelength to a desired range. While wavelength-shifters can increase the total luminescent output, each stage in the energy transfer chain may exhibit changes in pulse shape that make process modeling or consistent measurements difficult to achieve.

Material stability: qualities of the scintillator in terms of resistance to large radiation dosages and environmental factors. Properties that promote material degradation (*e.g.*, photobleaching, vibrational sensitivity, hygroscopicity) limit the detector's useful lifetime until replacement is necessary. This should be considered as a financial modifier when designing low-cost installations.

Structure: the physical qualities, other than stability, which recommend or discourage a material for a particular project. These include the maximum production size and shape of a scintillator block, the effective density for absorbing the targeted radiation type(s), and the clarity of the material to emitted secondary photons. Low values in these areas will generate poor results; if the path through the detector is insufficiently long enough for the radiation to fully deposit its energy, there will be pile-up at some level, as

higher-energy events are shunted into a single bin. Low transparency reduces the number of photons that reach the PMT, giving poor energy resolution, missed events through longer deadtimes, or electronic pulses that trail on and make consistent integration impossible.

Detailed below are those scintillators most relevant to the goals of our project, as well as the particular electronic and physical properties that guide our evaluation. Chapter 3 details the preparation of our own nanoscintillators, with testing results provided in Chapter 4.

### *2.1.1 Plastic Scintillators and Dyes*

An ideal choice for low cost or large format operations, plastic scintillators are formed by molding and curing an organic monomer into some desired shape. Some large-volume applications may begin with a block of already-cured polyvinyl toluene (PVT), poly(methyl methacrylate) (PMMA), or other plastic matrix, then use milling techniques to produce a final product of particular morphology. Typically, the scintillation from the base plastic is very low and this component is selected for optical clarity, ease of forming, or refractive-index matching with other elements of the detector system. For commercial or large-scale applications, a manufacturer will introduce a scintillating dye to encourage emissions from the plastic paddle or block.

Many of the dopants for plastic scintillators come in the form of organic dyes, such as 2,5-diphenyloxazole (PPO) or 1,4-bis(5-phenyloxazol-2-yl) benzene (POPOP). PPO occurs most commonly in conjunction with PVT, since its structure contains two phenyl rings, leading to high solubility in toluene and toluene-based solvents. POPOP, as a secondary scintillator, converts short wavelength light from near-UV (~350 nm) to a broad violet band around 410 nm. By exploiting energy transfer mechanisms, a scintillator can create a cascade effect from toluene to PPO to POPOP which moves the output wavelength into a high-sensitivity region for a particular PMT and increases total intensity by a large factor[8]. If an additional, gamma-sensitive nanoparticle component with matching initiator wavelength is added, its total luminescent output would be likewise amplified.

For the long-chain molecules in organic scintillators, the electrons which respond to ionizing radiation are not bound to a single atom, but are typically contained in a hybrid-shell system shared by several atoms in its vicinity. Hybridized molecular orbitals still have a defined energy range, but that value

can be tempered by the surrounding electronic systems and the vibrational level of the electron; this results in an electronic band structure, similar in appearance to that found in crystals and semiconductors, but different in operational principles. In consideration of the requirements for radiation detection, broad bands are typically not a hindrance, as long as the wavelength spread is in a high quantum-efficiency range of the accompanying photomultiplier or photodiode.

The cost of plastic scintillators is very low, but they are hindered by low sensitivity to high-energy gamma rays, poor linearity, and low tolerance to integrated radiation dosage. As each gamma passes through, the long-chain bonds are disrupted by the deposition of energy in the material. Over time, the structure accumulates a greater and greater number of defects, visible as discoloration of the plastic block. The color change not only affects the transmission of scintillation light, but indicates a reduced luminescent output – fewer intact  $\pi$ -bonds are available for the detection effect. Over time, the physical structure of the plastic reaches a failure mode, and with enough incident radiation, the surface will craze and the core will begin to crumble to dust. The amount of deposited energy to reach this point is quite high, but any installation using these materials should account for replacement costs in recognition of the degradation factors, as well as keeping the loss of detector efficiency under consideration.

### *2.1.2 Liquid Scintillators*

Another application for scintillating dyes lies in liquid-phase detectors. These materials forego the semi-rigid organic matrix of a polymer and simply suspend the luminescent dye in solution. As with plastic scintillators, organic solvents containing ring structures, like benzene, toluene, and naphthalene, have been extensively used in the sample-and-scintillator cocktails; work has proceeded in the search for effective combinations that require less-hazardous solvents. The foremost application for liquid scintillation counting is measuring the activity of other liquids, since proper solvent and fluor selection allows the sample under test, whether blood, water, or other fluid, to be directly mixed with the scintillation counter liquid. While liquid scintillators have excellent beta detection capability, and are quite useful in measurements of other liquids, the long energy transfer chains, concentration quenching effects, and often-dangerous solvents reduce their suitability for use in gamma scintillation systems.



### 2.1.3 Quantum Dots

Semiconductor constructs can leverage the change in properties between the macro- and nano-scales to produce luminescence. Some compounds, ZnO among them, do not produce luminescence in bulk form, but as particle size decreases, the dominance of quantum-mechanical effects becomes evident. Below  $\sim 10$  nm, a phenomenon called “quantum confinement” restricts the possible states available within the energy bands of the semiconductor crystal. As electrons are excited between the valence and conduction bands, they form electron-hole pairs called excitons. If the size of the quantum dot (QD) is reduced to less than the exciton Bohr radius – a measure of the orbital distance between the electron and hole – the particle’s luminescent properties take their cue from the limited allowed waveforms and the width of the band gap. Typically, size can be controlled by adjusting the synthesis reaction temperature or duration, or by depositing the structures through molecular beam epitaxy[9]. QDs in liquid scintillators could be used for radiation detection; however, this method would couple the downsides of liquid scintillators with the low gamma response of QDs and the enhanced environmental hazards of cadmium, a common component.

### 2.1.4 Commercial Single-Crystals

Currently, single crystals of Na(Tl) or CsI(Tl) are among the most widely-used commercial scintillating materials, even with increased application of plastics for large-format installations. These two compounds are chosen for a balance of the ideal measurement properties, as described above in this section’s introduction. The electronic structure for an alkali halide typically results in a band gap too large to produce the visible photons preferable for PMT detection. The addition of thallium or other elements, selection depending on the crystal host, acts to disrupt the electronic band structure and allow faster decay routes or emissions tuned to a particular wavelength. A particular crystal may be manufactured with certain measurement goals in mind; for two crystals produced by Saint-Gobain and used in our lab, NaI(Tl) has a higher photoelectron yield (from gamma ionization) and faster decay, but CsI(Tl) possesses greater light output per  $\text{keV}\gamma$  and is significantly less hygroscopic[10,11]. Recent work has explored the possibility of using  $\text{LaBr}_3$  or  $\text{LaCl}_3$  with a wide selection of additional rare-earth dopants[12,13]; these crystals have even greater gamma luminescence, shorter decay times, and higher resolution, but are also absorb atmospheric moisture with great alacrity, greatly reducing their ability to face the rigors of an uncontrolled environment.

In addition to the cost of growing a pure, single-phase crystal, the tendency to absorb water is one of the greatest barriers to their use. However, the performance of crystal scintillators is an important benchmark for new materials, and the industrial production of NaI, CsI, YAG, and others is robust and standardized for simple installation.

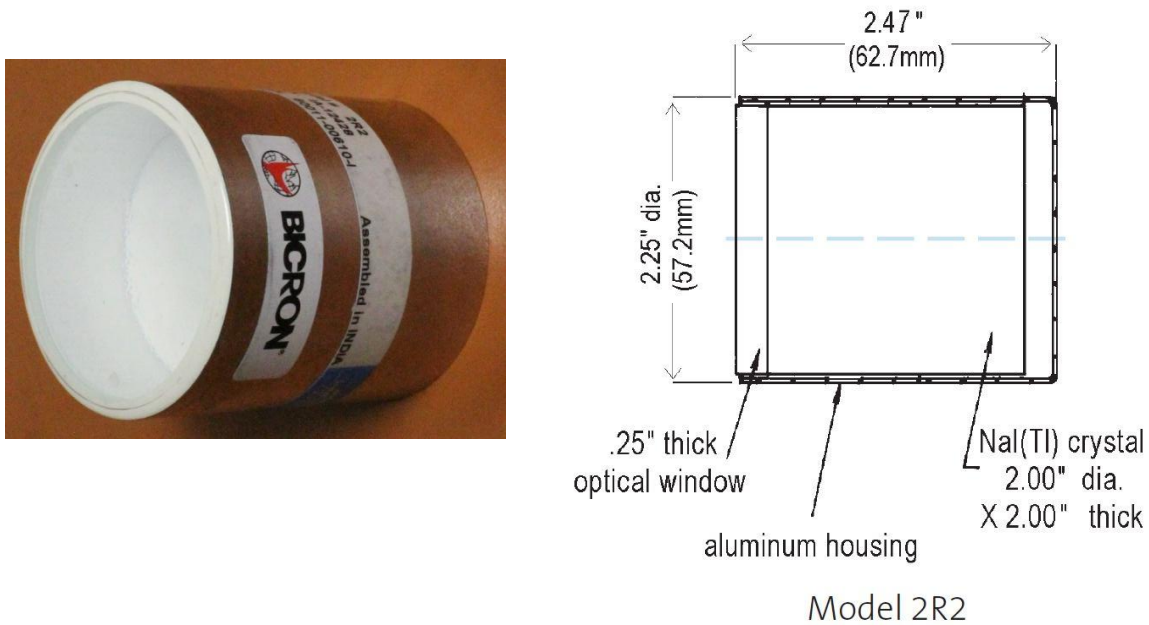


Figure 2.2: Bicron NaI(Tl) commercial scintillator.

The left image is our 2R2 model packaged scintillating crystal. On the right is the schematic provided by Saint-Gobain Crystal, the manufacturer, in their specification sheet.

#### 2.1.5 Comparison with Nanoparticle Scintillator Materials

A single-crystal detector is only sensitive to medium boundaries at a limited surface area. Typically, the face against the PMT window has a smooth, continuous surface, and coupling is aided by the application of optical grease. Some light may be lost to the opposite face or sides of the crystal, but coatings of Teflon tape or reflective material (see Figure 2.2) increase the quantity of incident light that is eventually directed into the PMT. For an assemblage of nanoparticles, even those in PVT, PMMA, or other matrices, each inter-particle gap represents at least two transitions in materials of disparate refractive indices; this often leads to a visible loss of transparency and the scattering of light throughout the material.

The result of this is that NP samples must produce an immense number of scintillation photons to overcome the scattering and trigger an appropriate count from the PMT/MCA.

One solution is to attempt matching indices between NPs and an organic or glass matrix. While sound in principle, this procedure introduces a new set of difficulties. Many inorganic scintillators require a high-temperature synthesis route, reducing their capability of accepting surface modifications. Without adjustment of their outer bonding structures, the particles aggregate in monomer precursors, curing into an opaque product, or one with a very low NP loading level, and subsequently dim luminescence.

An alternative to organic embedding is to use the NPs as components in a transparent ceramic construct. Though this method no longer technically generates a nanoparticle product, it would allow precursor particles to be grown to small diameters with wet-chemistry or glycothermal methods, then compression and curing of the resulting powder phase into a solid sample. Even though the synthesis process requires additional steps beyond simple nanocrystal production, it significantly reduces the need for an additional binding factor in the composite; some reports have indicated better transparency with the addition of ~0.01 wt.% MgO to fill interstitial spaces[14], but still achieved high clarity without MgO and high response with its inclusion. The final product retains the convenience and low costs of small-component growth and incorporates the fully active volume – and reduced grain boundary crossings – of a single crystal. Some work has already been performed to consider this route for Nd:YAG lasing material, with promising results[15]. By beginning the compression with stabilized YAG particles <200 nm, cold isostatic pressing forces continuity at the grain boundaries; the process achieves increased clarity over those using micron-diameter and larger particles.

## 2.2 Operating Principles of Radiation Detectors

While the materials and electronics commissioned for detector work have advanced significantly since Becquerel's work with photographic plates, modern systems follow a few schema quite similar to their early counterparts. In each case, the detector configuration aims to convert the incident radiation from alpha, beta, or gamma emissions to a signal readable by machine and interpretable by an operator. The design goals for the various detector types derive from what capabilities are most important. Some are designed for low-cost applications, where dead-time, energy discrimination, and particle identification are

irrelevant and ease-of-use and support simplicity are the dominant concerns. Others must distinguish between beta, gamma, and neutron radiation, or have high energy resolution for spectroscopy. One of the materials studied in this project has not been shown to produce a photopeak in nanoparticle form, but is highly responsive to absorbed dose; using this material in a portable rate measurement device may provide a more sensitive measurement and faster indicators of a dangerous radiological hazard.

### *2.2.1 Geiger-Müller Tubes*

Proposed by Hans Geiger, and refined with help from Walther Müller in 1928, G-M tubes are a simple system for basic radiation counting[16]. This device can indicate the passage of incident radioactive emissions, including  $\alpha$  particles if a sufficiently thin end window is used, by measurement of an output electrical pulse. The main body of the device is a cylindrical tube filled with low pressure inert gas; the walls and a thin axial wire are conductive, and a potential applied between them creates a strong electric field which encourages the drift of free charged particles. When ionizing radiation passes through the gas, its interaction with the widely-spaced molecules ejects a shower of electrons, often producing  $10^6$ - $10^8$  electrons from a single event. This interaction is most efficient near the central wire, and triggers the largest Townsend avalanches. Photons produced from the original initiator, typically in the UV range, also travel along the axis of the tube and can trigger secondary avalanches, which in turn produce those of higher order. This phenomenon can raise the total electron output to  $\sim 10^9$  from a single event[17]. To end the measurement, the abandoned positive ions form a local region negating the applied field and quenching further avalanches. As the heavier ions near the cathode, they retrieve electrons and are reset for the next interaction.

The multiplication effect allows G-M tubes to produce very large voltage pulses from small incidents, but the quenching mechanism makes it impossible to quantify the energy of the initiating ionizing radiation. The time for recombination and full sensitivity to another event can also be quite long, reducing the tube's effectiveness in high-radiation areas. Since much of the signal generated arises from later avalanches, it is also infeasible to use pulse-shape discrimination or other methods to determine what type of radiation caused the counter to trigger. While inexpensive to construct, the lack of information

beyond count rate and its inaccuracy at higher rates limit the usefulness of G-M tubes for our target applications.

### *2.2.2 Proportional Counters*

Advancing beyond the standalone G-M tube, a proportional counter combines the principles of that device with an ionization chamber. The structure is the same: a cylindrical tube filled with reacting and quenching gases, with a thin central anode wire and a wall-plated cathode. The major difference lies in the operational process. For the G-M detector, the voltage must be kept near the Townsend avalanche point to ensure that each incident photon or particle produces a maximum disturbance; each avalanche propagates additional showers before recombination occurs. Proportional counters work at significantly lower voltage, so that avalanches only occur in the region very close to the central anode. In the volume of the cylinder further from the wire, called the ion drift region, the field is low enough that incident radiation simply ionizes the contained gas. Each ion pair then “drifts” apart to the anode or cathode and, in the ideal case, produces exactly one avalanche near the anode. Since the ionizing radiation produces ion pairs proportional to its energy, a successful count of the avalanches will give an indication not only of the passage of a high-energy beta particle or gamma ray, but some measure of its energy as well.

Spectroscopic capabilities make the proportional counter vastly more useful than G-M tubes for applications of nuclear spectroscopy. The gas contents can also be adjusted for measurements of low energy x-rays ( $\sim 10$  keV). However, even with the influence of empirical normalizing effects, the number of avalanches detected is not exactly proportional to the quantity of ion pairs generated by the passage of radiation. This phenomenon results in poor detection linearity, giving a low precision in energy measurements at higher levels, around 14-17%, and can cause additional problems as the detector systems age or the ratio of contained active and quenching gases fluctuates[18].

### *2.2.3 Semiconductor-based Detectors*

Significant work has also begun to expand the use of semiconductor materials, which convert incoming photons directly into electrical signals by means of an array of reverse-biased diodes. Silicon-based installations currently in use at CMS, ATLAS, and other particle detector research facilities provide significantly higher tracking resolution than older wire chambers or their older counterpart cloud chambers.

Despite the measurement advantages, these detectors require extensive cooling to reduce electrical noise; without this refrigeration, the diodes suffer leakage currents which interfere with data accuracy. Additionally, the silicon microstrips lack radiation hardness, and lose operational capacity under prolonged exposure.

Another material, high-purity germanium (HPGe) may provide a response to some of these issues, but the associated technologies have not yet reached a point where replacement of most existing detector facilities is feasible. Achieving the necessary level of purity has only been possible within the last several years. HPGe requires cooling down to liquid nitrogen (LN) levels – approximately 100 K – to fully reduce source noise to acceptable levels. While thermo-electric cooling systems can replace actual LN, and refinements in purification technique can produce germanium products comparable in size to CsI or NaI, the cost for these processes is exceptional, with a representative model from Ortec at \$132,000 or more[19].

#### *2.2.4 Scintillation Counters*

Scintillating counters hold the position of greatest importance in regard to our research, since they combine gamma sensitivity with spectroscopic abilities. The earliest scintillating counter was Crookes' simple ZnS-coated screen, observed through a microscope, and limited by human visual acuity to about one detection per second[20]. Unsurprisingly, ZnS and other zinc-containing materials remain compounds of interest for nanoparticle scintillators, especially for in vivo applications. However, this work does not cover their synthesis and use, focusing instead on the commercial crystals used for scintillating detectors and our prospective nanoparticle replacements. These detectors are more suitable than ionization counters for field measurements of the gamma emissions from potentially hazardous radiation sources. Unlike G-M tubes and proportional counters, scintillating detectors do not directly convert incident radiation to an electrical signal. Instead, an incident photon passes through the medium, disrupting the electrons in the crystal structure. As the system returns to the ground state, the energy deposited in various levels of the electron shell is released, generally through emission of a series of photons, and the luminescent portion can be measured; a more detailed description of this process will be provided in section 4.1.2. For purposes of nuclear material identification and forensics, we desire materials with a strict relationship between incident energy and number of emitted photons. Without a linear response, it is difficult to correctly produce

photopeaks from the PMT and other downstream electronics, and the detector has little more use than a general counting system.

In addition to their spectroscopic properties, scintillating detectors enjoy broad adoption and much of the requisite technology is mature, making them a logical launching point for next-generation materials and prototype detector configurations. By advancing PMT technologies for greater sensitivity and improved signal-to-noise ratios, then coupling those devices with materials with higher, more finely-tuned luminescence properties, the overall detection efficiency can be increased. The result is a system which can detect smaller quantities of radioactive materials, or gamma emitters that have been shielded enough to hide from current scanning technologies; the detector could also generate a precise spectral profile of the radionuclide, separating a car with a  $^{99m}\text{Tc}$  medical isotope treatment from a truck carrying  $^{235}\text{U}$  disks hidden in discarded engine blocks.

### 2.3 Energy Transfer Techniques

To produce maximum emission intensity from a scintillator, or to tune the output wavelength to a high-sensitivity PMT wavelength range, we considered the use of energy transfer from the first stage scintillation components, typically the heavy rare earths in the host and dopant, to a secondary emitter. This process may proceed through a few different routes, each with its own requirements for spectral overlap or molecular structure. In a crystal system affected by the particular electronic energy level constructs introduced by a dopant ion, the emission spectra are subsequently affected, especially when overlap conditions are met between excitation and emission peaks. Most significantly, this alters the band gap to allow photoluminescence response in materials that otherwise would not absorb photons in the near-ultraviolet and visible ranges.

The key quantity for calculating efficiency is a simple ratio of the emission intensity of a certain molar quantity of isolated donor material to the emission intensity of that quantity of donor with the acceptor present. That is,  $I = 1 - (I_{DA}/I_D)$ , where  $I_{DA}$  is a particular peak's emission intensity with both the donor and acceptor present, and  $I_D$  represents that peak's value with only the donor under test. Higher energy transfer efficiency indicates good conjugation (for bonded nanoparticles) or proper size-controlled wavelength tuning (for all types).

### 2.3.1 Luminescent Energy Transfer

This is the simplest method to employ, both in terms of mechanism and synthesis conditions. In short, the first-stage scintillating compound, also termed the donor, is excited by a gamma event, then immediately decays back to its original state with the emission of a photon. The secondary emitter, designated as the acceptor, absorbs this photon with concomitant electronic excitation, then de-excites at its own characteristic wavelength. There are no distance restrictions on this operation, save those introduced by electronic influence from the surrounding matrix. In fact, the greatest hindrance to luminescent transfer is poor overlap between the donor emission and acceptor absorption; without proper matching, the first-stage scintillation photon is scattered or reabsorbed to affect crystal bond length or raise the vibration energy of the crystal.

In most composite materials with defects or doping centers, some of this phenomenon is offset due to a difference between the absorption and emission spectra. While an idealized, single-atom system should not see a shift between these wavelengths, thermal effects and crystal asymmetry result in a red shift in most materials, an effect called the Stokes shift; others may see a blue shift through photon upconversion or crystal cooling, with the corresponding name of anti-Stokes shift. Due to this process, the energy emitted by the donor is lower than its own peak excitation wavelength, which helps to promote light output by preventing reabsorption. In the composite material, the acceptor ion should be matched with the Stokes-affected emission of the donor, and the host material as a whole should be transparent to both the excitation and emission wavelengths of the donor.

Particle size also plays a role in luminescence transfer efficiency. Nanoparticles, especially those less than 100 nm, are subject to Rayleigh scattering; larger particles, while not appropriately called “nano”, are affected by its more precise generalization, Mie scattering. The Rayleigh scattering process is described by the following equation (for unpolarized light):

$$I = I_0 \cdot \left( \frac{1 + \cos^2 \theta}{2R^2} \right) \cdot \left( \frac{2\pi}{\lambda} \right)^4 \cdot \left( \frac{n^2 - 1}{n^2 + 2} \right)^2 \cdot \left( \frac{d}{2} \right)^6$$

where  $I$  is intensity of the scattered light,  $I_0$  and  $\lambda$  are the intensity and wavelength of the incident light,  $\theta$  is the scattering angle,  $n$  is the refractive index of the nanoparticles, and  $d$  is the NP diameter. In this range, it



is apparent that the intensity of the scattering is strongly dependent on the size of the nanoparticle; although the samples we prepared are not in solution, this effect is pertinent to suspensions in organic polymer hosts. With a small size, the scattering efficiency is very low, allowing a greater portion of the photoluminescent output to successfully pass out of the material.

The last factor controlling energy transfer success in this process is particle dispersion. While excellent luminescent emission can be achieved from samples with high relatively particle density, it is critical to attempt a homogeneous particle distribution in the organic host. One issue we have faced with polymer embedding is that many synthesis routes, through either solvent adsorption or high temperature requirements, preclude the use of organic surface modifiers without additional processing. A shell compatible with the benzene structures in PVT can be applied, but typically quenches emissions by providing additional, complex electron structures which permit non-luminescent energy transfer. Without this coating, however, the NPs tend to aggregate within the organic monomer before the polymerization linkage can proceed and hold them in place. The result is a sample with high clarity (but no nanoparticle doping) in some regions, and opacity from agglomerated NPs in others—and poor luminescent qualities in both types.

### *2.3.2 Förster Resonance Energy Transfer*

Also known as FRET, this phenomenon is often confused with luminescent transfer due to the similarities in their prerequisites. In fact, the two interactions have been studied as the long- and short-distance analogs of a single phenomenon, through principles of quantum electrodynamics[21]. Unlike luminescent transfer, the chromophores in a resonance transfer system exchange energy through dipole-dipole coupling, not absorption and re-emission, in a process called inter-system crossing (ISC). Thus, the efficiency of the interaction depends not only on donor-acceptor separation, but on the orientation of the two components' dipole moments. The complex electronic structures of rare-earth ions allow for a complex dipole structure and can enhance the rate of FRET emissions. Also, in this case, the physical separation of the donor and receiver in the ISC is much lower than the wavelength of the exchanged virtual photon. Thus, the process only occurs when the participants are very close, at ~10 nm separation, and it is

extremely dependent upon this radius. With increased interparticle distance, the efficiency of the interaction drops off as  $10^{-6}$ , until the process transitions to the luminescent transfer regime.

Other non-radiative factors can affect the efficiency of visible light output. Another factor, similar to inter-system crossing, is internal conversion (IC). Here, the electron shift does not change the spin state for the molecule, but the excess energy and momentum are delivered into the crystal matrix as heat. The Franck-Condon principle also describes the loss of some luminescence; this concept incorporates the vibrational modes of fluorescing molecules in the crystal into the energy change seen in the Stokes shift (and its short-range analog). Here, nuclei of an affected molecule do not have sufficient time to reach equilibrium after a shell electron absorbs a photon and moves to the conduction band ( $\sim 10^{-15}$  s). The shift in the electron shell coupled with Coulombic interactions with the surrounding crystal matrix results in a change in the equilibrium position, requiring several picoseconds for the system to relax to the lowest excited vibrational state. Kasha's rule states that fluorescence emissions occur almost exclusively when the molecule is in its lowest vibrational energy state, regardless of other electron energy considerations. For our scintillators, energy transfer through vibrational relaxation can move the wavelength of the last-stage fluorescence emission out of the visible range and the ideal range for the PMT.

## Chapter 3

### Materials and Synthesis Procedures

While organic materials have their own advantages for radiation detection as discussed above, this project focuses primarily on inorganics, to employ their physical stability and increased radiation resistance. For the early stages, we studied a variety of materials to determine whether it were possible to convert applications with bulk scintillators to nanoparticle counterparts. In many cases, industrial synthesis of the bulk crystal requires exceptionally high temperatures, which lead to large grain sizes; for a single-crystal application, this is desirable, since minimizing grain boundaries increases transparency, and defects in the lattice structure may have unintended emissions or varying levels of response that affect the precision of an instrument. However, to exploit the particular qualities of nanoparticle scintillators, we required adjustments in the synthesis routes that allowed surface modification, particle size control, or easy sonication of the final product to sizes less than 200 nm. Basic production methods for the different materials are briefly described, along with the modifications necessary for our purposes.

#### 3.1 Lanthanum Fluoride

Cerium-activated  $\text{LaF}_3$  exists in nature, albeit in a highly impure form, as the mineral fluocerite. However, it wasn't until 1990 that single crystals produced by the Bridgman technique (differential cooling around a seed crystal) reached sufficient properties of purity and size to warrant in-depth study of its scintillating properties[22]. Although the luminescent output of  $\text{LaF}_3\text{:Ce}$  is lower than other scintillators—giving approximately 2.2 photons/keV, while  $\text{NaI(Tl)}$  gives  $\sim 38$   $\gamma$ /keV—it is not hygroscopic and has a very fast, 3.0 ns emission component. It can also be produced in nanoparticle form through a variety of synthesis methods, making it an ideal candidate for exploration as a spectroscopy-enabled nano-scintillator.

##### *3.1.1 Solid State Diffusion*

We first attempted production of this material in nanocrystal form through a typical solid-state diffusion (SSD) method. The reagents are shipped and stored as crystalline powder, with a grain size of 1-2 mm. To promote a homogenous reaction, stoichiometric amounts of  $\text{NH}_4\text{F}$  and  $\text{La}(\text{NO}_3)_3 \cdot 6\text{H}_2\text{O}$  were added to a mortar and pestle, then mixed. Small amounts of water and heat were produced as the reaction between

fluorine and the metal groups proceeded at a low level, and additional deionized water was added to maintain a thick, white paste. Grinding continued until the paste was visually and haptically smooth, then it was transferred to a small crucible with lid. The sample was placed in a muffle furnace set to 700°C for 4-6 hours, depending on experimental timing conditions, then allowed to cool in the oven to room temperature. Once cool, a rough plug of bonded  $\text{LaF}_3$  was extracted and ground for 10 minutes to acquire a fine powder, which was stored in glass vials in a closed box to prevent possible photobleaching.

For samples doped with an additional rare-earth activator, measured amounts of  $\text{Ce}(\text{NO}_3)_3 \cdot 6\text{H}_2\text{O}$ ,  $\text{Tb}(\text{NO}_3)_3 \cdot 5\text{H}_2\text{O}$ , or  $\text{Eu}(\text{NO}_3)_3 \cdot 5\text{H}_2\text{O}$ , for cerium, terbium, and europium doping, respectively, replaced the  $\text{La}^{3+}$  source to maintain a 1:3 ratio of rare-earths to fluorine. For instance, a sample with 96:3:1 doping (La:Ce:Tb) and final mass of ~2.00 g would contain 9.8 mmol lanthanum nitrate, 0.31 mmol cerium nitrate, and 0.10 mmol terbium nitrate combined with 30.63 mmol ammonium fluoride. The total molar ratio of rare-earth to fluorine is then precisely 1:3.

This solid-state method produced samples with strong green photoluminescence as shown in Figure 4.4. By adjusting the doping concentration range for each additional component from 1 mol% to 10 mol%, we were able to construct optimum luminescence output values. The colored inset boxes in that figure show the integrated intensity across the UV-visible range. For radiation detection, it is critical that the emissions match the detection range of the PMT, which loses sensitivity in very short and very long wavelengths. As long as the incident photon falls in this range, even materials which lack sharp emission peaks may be promising scintillators, if the integrated intensity is high in wavelengths appropriate to the PMT's quantum efficiency plateau.

### *3.1.2 Wet Chemistry*

Investigating the literature to seek methods for decreasing particle size for better solubility and surface modification, we explored the use of wet chemistry synthesis for doped  $\text{LaF}_3$ [23]. By suspending the reagents in an alcohol or aqueous phase, the active surface-area-to-volume ratio is increased, and the interaction should proceed more homogeneously throughout the medium. In contrast, even with the slight amount of  $\text{H}_2\text{O}$  evolved through grinding at the pre-sintering stage, the solid state method does not achieve full suspension of the components, and occurs at such high concentrations that equal distribution of seed

crystals is unlikely. For the wet chemistry procedure, the fluorides and nitrates are measured as above. Ammonium fluoride is placed into methanol or ethanol at a concentration of approximately 30 mg/ml or 22.5 mg/ml, respectively. The combined rare-earth nitrates are also placed into a separate alcohol solution, with 890 mg/ml (MeOH) or 356 mg/ml (EtOH). The fluoride solution is heated to just below the boiling point of the alcohol (MeOH to 65°C, EtOH to 75°C), then the nitrate solution, maintained at room temperature, is added drop-by-drop, at a rate of 2 ml/min. Additional alcohol was used to rinse the nitrate solution beaker, then this rinse added dropwise at the same rate. The solution was heated to 78°C, the boiling temperature for pure ethanol. However, the solute and dissolved water increase the boiling point above this level, so the sample evaporates quickly but not violently.

### 3.2 Yttrium Aluminum Garnet

Yttrium, aluminum, and oxygen can combine into three distinct crystal structures: monoclinic (YAM, formula  $Y_4Al_2O_9$ ), perovskite (YAP, formula  $YAlO_3$ ), and garnet (YAG, formula  $Y_3Al_5O_{12}$ ) phases. The first two, YAM and YAP, may be synthesized at lower temperatures; however, they lack the desired luminescent properties found in the garnet, due to a combination of all three phases in various crystal grains. YAG has been employed in a variety of optics and sensing application, including Nd:YAG and Ho:Cr:Tm:YAG as active lasing materials[24], Dy:YAG for temperature sensing[25], and Ce:YAG for lighting[26]. Laser cores require a very fine emission band structure and proper positioning of metastable states, so nanoparticle composites are less useful in this area. However, for lighting, temperature sensing, and radiation detection, using nanoparticles provides opportunities for a combination of improved sensitivity, reduced costs, or better miniaturization capabilities. YAG production may follow several different routes, but each seeks to apply formation conditions that push YAM and YAP to reconfigure into the garnet phase while maintaining smaller particle sizes.

#### 3.2.1 Solid State Diffusion and Combustion Methods

The simplest method for producing single-phase YAG is solid state diffusion. As with  $LaF_3$ , it is difficult to control the size of particles produced with this method, and any surface modification must be done after sintering. Additionally, the greater temperatures exceed the limit for a typical porcelain crucible; the reaction vessel must be composed of alumina or zirconia. However, SSD has the advantage of extreme

procedural simplicity:  $\text{Y}_2\text{O}_3$ ,  $\text{CeO}_2$  and  $\text{Al}(\text{OH})_3$  are mixed in appropriate molar ratios ( $\text{Y}:\text{Ce}:\text{Al} :: 3-x:x:5$ ), placed in a crucible, and heated to near the YAG melting point. Depending on reactant particle sizes, lower temperatures (1000-1500°C) will result in a mix of YAM, YAP, and YAG or require exceptionally long sintering times. For sub-micron reagents, the proximity of the reactant ions is much greater, allowing YAG formation below the high-temperature range[27]. Due to the difficulty of producing homogeneously-sized nanoparticles with this method, the inability to apply surface modification during formation, and the high temperatures involved, our work does not consider solid-state diffusion as an option for nanoparticle formation. Particles  $<1\mu\text{m}$  may be formed from SSD products by processing with a ball-milling method, but this additional step also discourages the use of a diffusion method when other routes are more efficient.

### 3.2.2 Microwave Synthesis

To overcome the high-temperature requirements of SSD and provide a route for surface structures compatible with organic solvents or PVT, we attempted a synthesis using a microwave heating system. For several reasons discussed below, this route was not successful; however, the method is included here for a comprehensive view of experimental procedures. Additionally, this synthesis provided valuable information about the chemical processes that should occur at each stage of YAG formation.

First, 572.05 mg  $\text{Al}(\text{OCH}(\text{CH}_3)_2)_3$  (aluminum isopropoxide), 539.80 mg  $\text{Y}(\text{CH}_3\text{CO}_2)_3 \cdot 4\text{H}_2\text{O}$  (yttrium acetate), 32.56 mg  $\text{Ce}(\text{CH}_3\text{CO}_2)_3 \cdot 2.5\text{H}_2\text{O}$  (cerium acetate), and 12 mL  $\text{HO}(\text{CH}_2)_4\text{OH}$  (1,4-butanediol) were added to a 35 mL-capacity microwavable vial. The ratio between the yttrium and cerium compounds should produce a doping level of 5% by mole. A magnetic stirring system is used to suspend the powder components in the butanediol, then the stir bar is removed. The vial is capped and placed into the microwave system with a target temperature 300°C, power 50W, and pressure limited to 300 psi (2.07 MPa). After 120s of premix, the microwave cycle was begun. Initially, we intended to cycle the reagents for 2 hours; however, the temperature had only reached 195°C after one hour, and maintained a plateau at that point. After 75 minutes of microwave exposure, the power was increased to 200W. Even at this power, the microwave synthesis did not surpass 200°C and 107 psi. After three hours of total operation after premix, the reaction produced approximately 10 mL of a faintly yellow, milky suspension with solid white

deposits. Neither extracted suspension nor the white powder displayed any visible luminescence, indicating that the synthesis was unsuccessful.

One issue is that 1,4-butanediol is a nonpolar solvent, and has very little reaction to the microwave heating effect. Much of the early heating of the sample came from adsorbed water or trapped atmospheric moisture. Additionally, the reported glycothermal synthesis (discussed below), which formed a model for this experiment, required temperatures of 300°C and pressures nearing 4.5 MPa. Without the heating capability necessary to reach that temperature, and with pressure limited by the microwave-reactor release system to ~2 MPa, the reaction did not proceed.

### 3.2.3 Modified Glycothermal Technique

Working to overcome the issues with the microwave synthesis, we attempted another route designated as the modified glycothermal method (MGM). The result was a combination of principles from solvothermal and solution-gelation (sol-gel) methods. By assembling an organic suspension and forcing increased viscosity through dehydration before sintering, the initial small particle size should be maintained by limiting the reaction to small pockets of reagents within the gel, but the final reaction would take place under standard sintering after the seed crystals had formed in isolation. From early results and *post hoc* analysis of the incomplete microwave-induced crystallization, the process of MGM is the operational mechanism that should have occurred in the reagents and organic solvents.

As an example synthesis, 1.72029g aluminum isopropoxide were suspended in 5 ml each of 1,4-BG, poly(ethylene glycol)-200 (PEG-200), and isopropanol. Then, 1.83886g yttrium nitrate hydrate and 0.10972g cerium nitrate hydrate were added to 10 ml deionized water to attempt a YAG:Ce product at 5.0% doping. The aluminum-organic and nitrate solutions were separately heated with stirring to 60°C on hot plates, then held at that temperature for 30 minutes. The aluminum-organic suspension was then added dropwise to the nitrate beaker, using ~20 ml of isopropanol as a rinse. The mixture was stirred for an additional 30 minutes, then placed in a drying oven at 90°C for 24 hours. After the drying stage, the products had formed a yellowish, translucent paste, indicating dehydration and partial polymerization of the organic solvents. The gel was transferred to a crucible and heated at 600°C for 2 hours. The temperature was then increased to 900°C for 2 hours, then to 1100°C for a final 2 hours. The resulting product formed

several yellow-white, fragile aggregations that were easily crushed in a crucible and ground to a fine powder. Fluoroscopy testing, detailed in Chapter 4, showed excellent response, and this procedure was used as a benchmark for comparison measurements.

#### *3.2.4 Coprecipitation Method*

An additional tested synthesis used a solution of metal ions and a surfactant to control initial aggregation size, based on recent work[28]. Despite the promise of an ideal product, several factors made it difficult to produce consistent results, the procedure required a significant time, and the product did not outperform other methods. This mode was used for a few relevant samples, however, so in the interests of completeness, we have included it here.

Briefly,  $\text{Y}(\text{NO}_3)_3 \cdot 6\text{H}_2\text{O}$ ,  $\text{Yb}(\text{NO}_3)_3 \cdot 5\text{H}_2\text{O}$ , and  $\text{Al}(\text{NO}_3)_3 \cdot 9\text{H}_2\text{O}$  were dissolved in a stoichiometric ratio (2.85:0.15:5.0 by mole) in 200 mL deionized water, with an additional 1.82175g of sodium dodecyl sulfate (SDS) added. This solution is stirred at 400 rpm until all the nitrates are dissolved and the SDS is fully dispersed. A second solution containing ammonium hydrogen carbonate (AHC) at 0.5M in 115 mL DI water is prepared and heated to 50°C while stirred at 400 rpm. After 30 minutes of stirring, the salt solution is added dropwise to the beaker containing AHC. After the two solutions are fully mixed, they are stirred for an additional 30 minutes, then processed with a vacuum filtration system to remove most of the liquid. The remaining product is then rinsed with DI water and pure EtOH and dried in air at 60°C for 24 hours. This produces a whitish cake of SDS-covered nanoparticles, which are then sintered at 500°C for 3 hr, then 1050°C for 2 hours. After sintering, the white cake of easily-flaked material is broken up into small particulates through agate mortar grinding.

### 3.3 Strontium Fluoride

The utility of  $\text{SrF}_2$  compounds lies in a different area than gamma spectroscopy. As the material is exposed to an increased integrated dosage, the incident gamma energy forces changes in the crystal structure. These alterations should be evident when observing the photoluminescence and x-ray excited luminescence spectra over time. Using a technique called fluorescence intensity ratio (FIR) comparison, two or more peaks are considered; as total energy absorbed increases, the ratio of the peak heights changes. By calibrating a measurement against a source of known activity, the dose absorbed in a field trial or



radiation monitoring system can be extrapolated against the established FIR curves. Our results confirm that doped  $\text{SrF}_2$  exhibits both PL and x-ray excited luminescence, so those properties could also be exploited for a typical counting system as well. Based on encouraging results from our previous collaborative work[29,30], doped  $\text{MgF}_2$  and  $\text{CaF}_2$  are also produced as comparative elements, using the same synthesis methods and testing procedures.

### 3.3.1 Solid-State Diffusion

This method is appropriate for first studies of strontium fluoride; the synthesis is simple, quick, and it is easy to test the crystallization level and luminescence properties of the finished product. However, like other SSD procedures, the final particles may possess a large size variance, poor homogeneity in doping-element inclusions, and severe aggregation. Several other methods, notably a hydrothermal process[31], would be more suitable for further studies on  $\text{SrF}_2$ .

As a representative synthesis, 1,996.30 mg of  $\text{SrF}_2$  powder (2 micron nominal size) are added to 2.00 mg  $\text{MnCl}_2$  and 3.02 mg  $\text{EuCl}_2$  in a small beaker; the target results are dopant ratios of 0.1% and 0.085%, respectively. ~30 mL of EtOH is added, and the mixture is stirred at 300 rpm. A small glass rod is used to break up aggregations and ensure good suspension. After 1 hour of stirring, a flow of air is directed across the surface of the mixture, encouraging fast evaporation of the solvent. When the reagents have dried to an exceptionally fine white powder, they are removed from the beaker and placed in a small crucible. The initial oven temperature is set to 200°C to allow evaporation of adsorbed water and any remaining ethanol. After 1 hour, the temperature is increased to 500°C, then to 800°C after an additional hour. Some testing was performed at 4 and 6 hours sintering at the maximum temperature, but the samples aged for 4 hours ( $\text{SrF}_2\text{:Mn,Eu-v3}$ ) demonstrated better luminescence performance, shown in Figure 4.10. At the end of the sintering stage, the material is allowed to cool in the oven to room temperature, then is extracted and ground to a fine powder in an agate mortar. Table 3.1 below gives the synthesis conditions for selected samples of  $\text{SrF}_2\text{:Mn,Eu}$  and related group-2–rare-earth NPs.

Table 3.1: Synthesis conditions of selected SrF<sub>2</sub>, MgF<sub>2</sub>, and CaF<sub>2</sub> samples.

Sample Designation	Mixing Type (EtOH)	Mn mol%	Ce mol%	Eu mol%	Sinter Time
MgF <sub>2</sub> :Mn,Eu	Dry	0.15	--	0.56	4h
CaF <sub>2</sub> :Mn,Eu	40 ml	0.1	--	0.085	4h
SrF <sub>2</sub> :Mn,Eu·v1	Dry	0.1	--	0.085	4h
SrF <sub>2</sub> :Mn,Eu·v2	30 ml	0.1	--	0.085	6h
SrF <sub>2</sub> :Mn,Eu·v3	40 ml	0.1	--	0.085	4h
SrF <sub>2</sub> :Mn,Eu·v4	40 ml	0.2	--	0.17	4h
SrF <sub>2</sub> :Mn,Ce	40 ml	0.2	0.1	--	4h
SrF <sub>2</sub> :Ce,Eu	40 ml	--	0.1	0.17	4h
SrF <sub>2</sub> :Mn,Ce,Eu	40 ml	0.2	0.1	0.17	4h
SrF <sub>2</sub> :Mn	40 ml	0.1	--	--	4h
SrF <sub>2</sub> :Ce	40 ml	--	.1	--	4h
SrF <sub>2</sub> :Eu	40 ml	--	--	0.085	4h

### 3.4 Commercial Comparison: NaI(Tl)

This material was purchased from Saint-Gobain’s Bicorn brand of commercial scintillators and used as a normalization point for other samples. Solid crystals with this composition have been in use since about 1955, evolving as a high-efficiency alternative to scintillating screens suitable for use with newly-developed photomultiplier tubes. Our crystal follows the design shown in Figure 2.2, taken from the Bicorn line specification sheet and a photograph of our unit; the majority of the assembly is a monolithic NaI(Tl) crystal, with a thin aluminum and Teflon shell to reflect light toward the open face, which is then protected by a layer of glass. This type of construction allows precise matching with the PMT face through a thin coating of optical grease. Using a typical instrumental setup, we measured the PL and XL properties for comparison with our crystals (see Figure 3.1). Since the crystal structure is very regular, a sharp excitation peak is seen at 319 nm. While undoped NaI has a bandgap of 5.8 eV (~210 nm), the thallium activator introduces intermediate states for energy dissipation, leading to the broad emission from 330–500 nm. Under x-ray excitation, only the peak centered at 420 nm exhibits emission, but the large area under the peak gives an integrated intensity of over 140 kcps, even when using the small cone of sensitivity from the fiber optic collection system. Based on the evidence in Figure 4.8, our YAG:Ce produces a significant fraction of this light, but does not cover the area of the full commercial crystal.

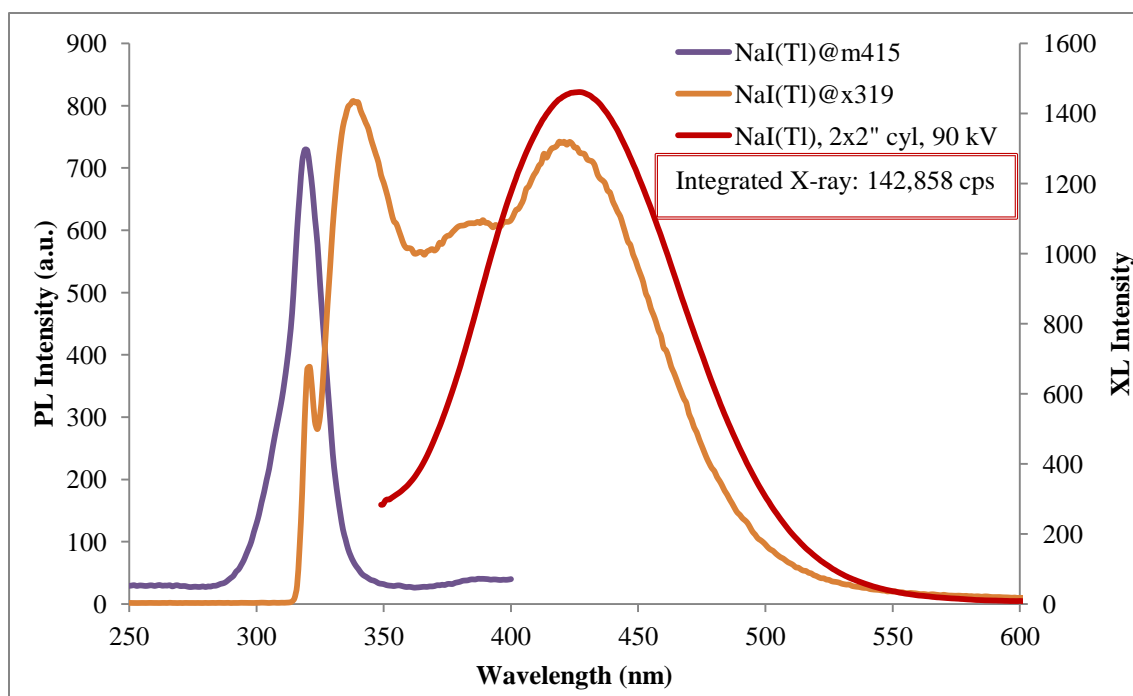


Figure 3.1: PL and XL of a commercial NaI(Tl) scintillator.

Shown are the narrow excitation band at 319 nm (purple) and the broad UV-vis emission between 330 and 530 nm. The red trace is the x-ray emission spectrum, totaling in ~143,000 cps (inset) when integrated from 350–500 nm.

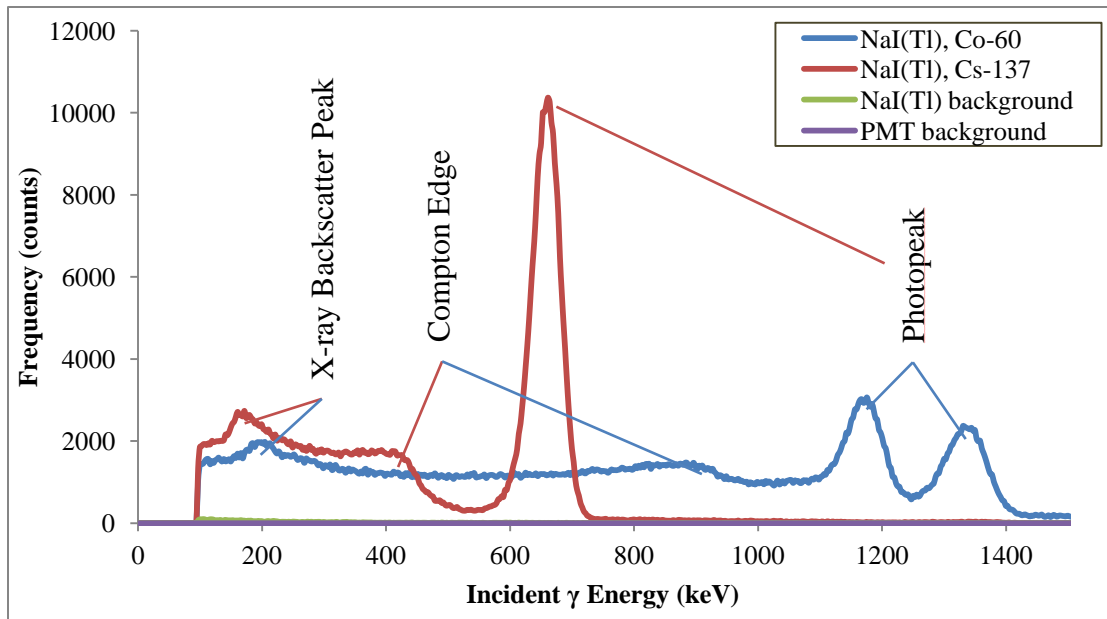


Figure 3.2: Gamma scintillation response of NaI(Tl) crystal.

Clearly evident are the x-ray backscatter peaks from the detector material, the Compton edge from elastic collisions, and the photopeaks generated by nuclear rearrangement.

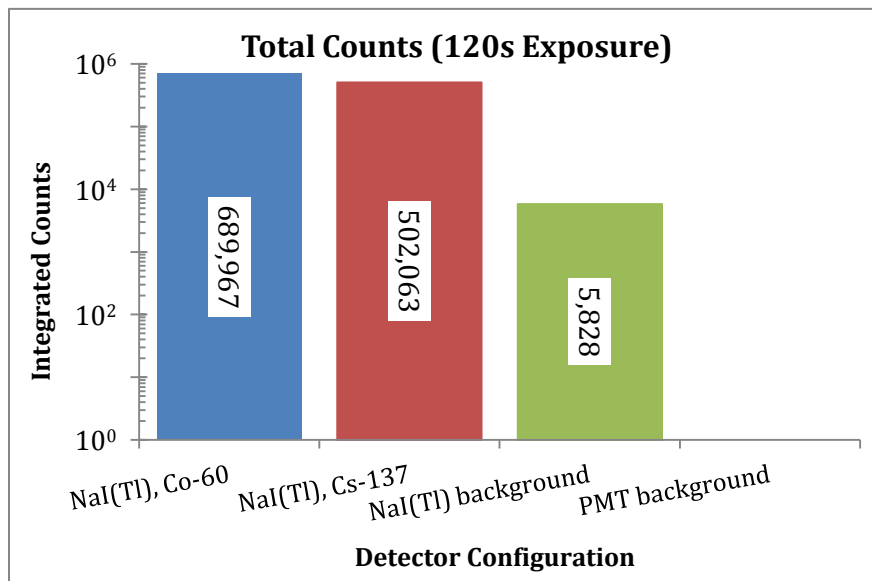


Figure 3.3: Integrated counts for NaI(Tl).

Without sources or scintillator present, detector response drops off sharply.

## Chapter 4

### Testing and Results

Evaluating a newly-synthesized material for gamma ray studies involves several stages of characterization and analysis. Weak performance in a particular area does not disqualify a particular sample from other testing, but rather provides a series of guidelines for improving synthesis procedures and refining techniques. Materials analysis covers several broad categories. The most important of these, in terms of suitability for our project, is luminescence performance, tested through photostimulated luminescence and x-ray excitation. The second aspect of import concerns structural and compositional scrutiny – what surface features do the products possess, how well-crystallized are the nanoparticles, x-ray powder diffraction (XRD) confirmation of composition, etc. The third tier examines the particles' physical suitability for real-world products for radiation detection applications. Visual examinations of transparency, scanning electron microscopy (SEM), high-resolution transmission electron microscopy (HR-TEM), and confirmation of performance with gamma activation in a typical gamma source / multi-channel analyzer (MCA) system. The individual techniques and the principles behind their operation are detailed below, followed by the results from each material. Additional information regarding default settings, resource identifiers, and other associated concepts is included in Appendix A.

#### 4.1 Characterization Techniques

##### *4.1.1 Photoluminescence Appraisal*

The primary indicator for determining material suitability for gamma spectroscopy is the material's photoluminescence (PL). The production mechanism of emissions from ultraviolet or visible is different from the higher-energy interactions of gamma rays, but the energy transition activated allows a first look at the material's ability to emit light and its transparency to those emissions. In our PL measurement system, light of a fixed wavelength is emitted from a monochromator system onto the exposed sample. An orthogonally-placed window allows the emitted light from the sample to enter a second monochromator, whose output is detected by a photodiode and translated into a relative intensity measurement. As shown in the sample spectrum, Figure 4.1, the data we present omit some points where

the intensity of the emitted light may become very high, especially at the reflection points, or regions where the measured emission wavelength equals that of the excitation source or an integer multiple of that value. These gaps are noted when they obscure features of the data, but are a consistent instrumental effect. Any points not included for reasons other than this instrument effect will be noted and explained in the accompanying text. This figure also represents the general mode of presenting photospectroscopic data that will be used in the discussion of other materials. Data concerning the excitation spectra, indicating which

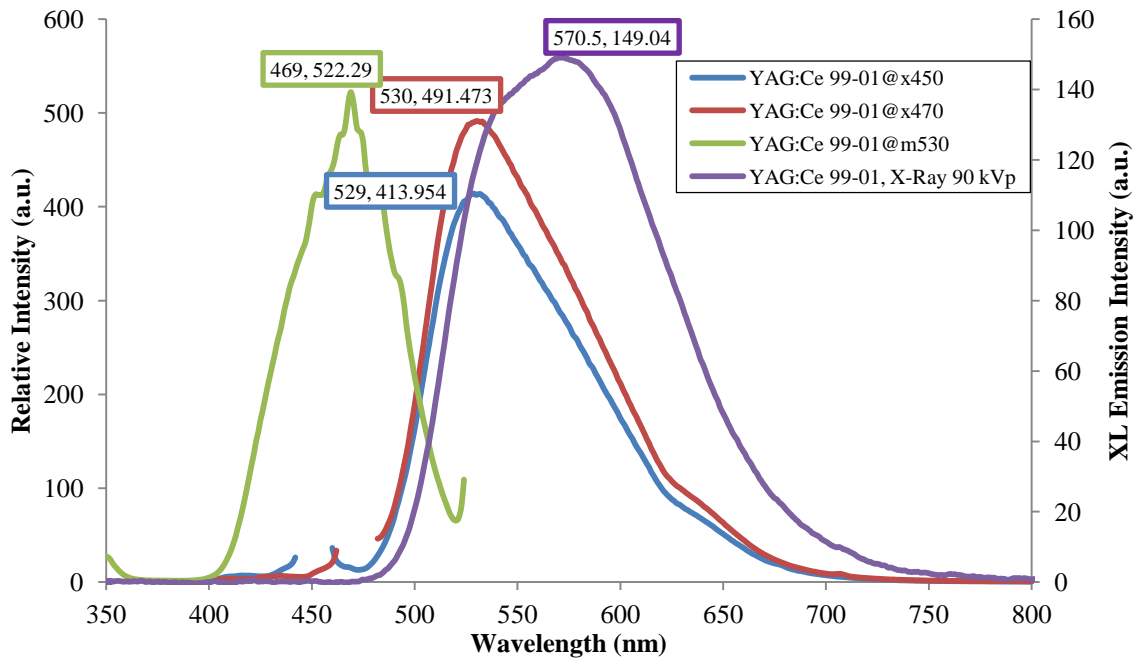


Figure 4.1: Sample photoluminescence and x-ray luminescence spectra.

The green trace is the excitation spectrum at the peak emission value (530 nm); red and blue show emission spectra under two separate excitation wavelengths. The purple blocked line represents x-ray scintillation response. Gaps near 450 (blue line) and 470 (red line) result from the omission of out-of-scale data from excitation source reflection points.

wavelengths excite the sample most efficiently, are labeled with “m530” or some other number, indicating that the excitation source scans through a range of wavelengths and output is measured at a fixed emission wavelength. Likewise, “x450” and similar labels indicate a fixed excitation energy, and a scan in the

emission space. As discussed in the next section, the x-ray excitation spectra differ somewhat from the PL mechanism.

The physical principle which results in a PL emission is a simple excitation of an outer-shell electron, followed by relaxation and re-emission of a photon. Due to the nature of the bonds in inorganic compounds, the emitted photon is typically at a longer wavelength than the absorbed photon; this effect, called the Stokes shift, arises when energy is dissipated through non-luminescent means. For our purposes, the non-radiative transfer in FRET is the most important component, since the inter-system crossing route results in an angular momentum transfer between resonant donors and acceptors.

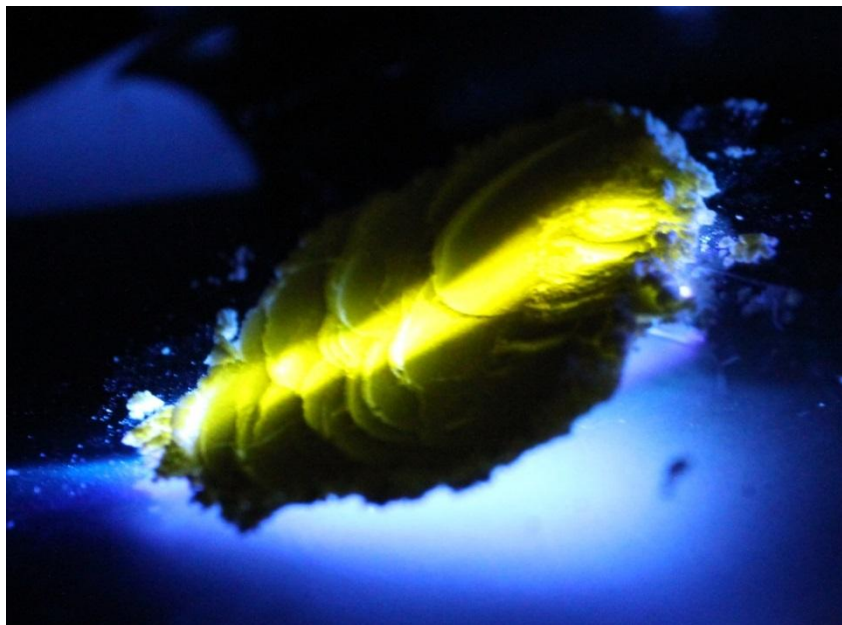


Figure 4.2: YAG:Ce demonstrating Stokes shift.

This 2 cm diameter sample of YAG:Ce nanopowder absorbs blue light and emits in the yellow-green region. Typically, the measurement is taken with a smaller, specific amount of product; here, a larger quantity is used in open mounting for visual demonstration.

#### *4.1.2 X-ray Excited Luminescence*

The energy of an x-ray photon is significantly higher than that of visible light; thus the process that drives x-ray excitation, as well as gamma scintillation, relies on a different mechanism from photoluminescence. A typical photon from the IR-vis-UV region carries about 1 to 5 eV of energy (from

1150 to 250 nm wavelength), which is a suitable match for the bandgaps of many semiconductors, insulators, and doped halides. A low-energy x-ray photon, however, may carry 100–200,000 eV before entering the energy regime reserved for  $\gamma$ -rays, though some older conventions specify different energy boundaries or differentiate based on production mechanism; x-rays are artificially generated through electron transitions near the nucleus or through Bremsstrahlung effects in matter, while gamma photons are produced from nuclear energy level shifts and particle annihilations. Regardless of terminology, when the energy of the photon reaches a sufficient level to completely remove outer- or inner-shell electrons, the incident photon is classified as ionizing radiation. Because both categories of photon affect the inner-shell electrons in a similar way, we may use x-ray luminescence (XL) testing as a guide to a particle's effectiveness in detecting  $\gamma$  photons.

Our cabinet x-ray system, a Faxitron RX-650, consists of a shielded enclosure coupled with an x-ray production system and fiber output. Samples are placed within the light-proof cabinet, irradiated, and the resulting light in the UV to NIR region is delivered to an OceanOptics QE65000 spectrometer. The spectrometer uses a Czerny-Turner type monochromator to separate the various incoming wavelengths onto a CCD detector; the output is displayed, analyzed, and saved through the manufacturer's software.

Due to the photon production mechanism, our x-ray apparatus does not generate a single-energy beam of x-rays; instead, electron diffraction through the tungsten target produces a spread of wavelengths up to a maximum energy set by the excitation voltage of the machine. Analysis of the energy distribution is beyond the scope of this work, but we have taken steps to minimize its effects. The machine is kept in proper calibration and the warm-up procedures are followed, both as recommended by the manufacturer. The samples tested are small compared to the beam diameter, and consistently placed; this results in little beam divergence between the target and sample, and limits the spread of incident photon energies from x-rays produced through off-axis target interactions. Finally, all tests are performed at an accelerating energy of 90 keV, well above the innermost K-shell edge of La at 38.9 keV, Ce (40.4 keV), Tb (52.0), or even Yb (61.3 keV), used in some YAG samples to experiment with NIR production). Altogether, these restrictions serve to produce consistent, comparable measurements of XL scintillation response



#### 4.1.3 Gamma Ray Stimulation and Scintillation Counting

Like XL, gamma luminescence involves interactions between photons and inner shell electrons of the scintillator atoms. The major difference is, depending on definition, either the energy level or the source of the incident photon, as described above. Our  $\gamma$ -radiation sources are calibrated amounts of radionuclides, specifically  $^{137}\text{Cs}$  and  $^{60}\text{Co}$ . The production dates for the sources used are August 2009 for cesium and May 2011 for cobalt; each was manufactured with an initial activity of 1  $\mu\text{Ci}$  (microcurie) or  $3.7 \times 10^4$  decays per second. Based on the standard activity-decay equation:

$$N(t) = N_0 \cdot (0.5)^{\frac{t}{t_{1/2}}}$$

where  $N(t)$  is the activity at a given time  $t$ ,  $N_0$  the initial activity, and  $t_{1/2}$  the half-life; half-life is specific to each isotope and represents the amount of time for one-half of the contained radioactive nuclei to decay into their daughter nuclides. For our two sources, the half-lives are 30.07 yr ( $^{137}\text{Cs}$ ) and 5.27 yr ( $^{60}\text{Co}$ ), so at the time of testing in March 2013, the activities of the sources are 0.9577  $\mu\text{Ci}$  and 0.7817  $\mu\text{Ci}$ , respectively. Our setup, shown below in Figure 4.3, does not hermetically cover the radioactive source, so our effective activity is much lower, at about 40% of the total value. The total radiation exposure also occurs at a much lower rate using gamma sources compared to the x-ray cabinet irradiation system; thus, a much longer integration time is used to collect data with radioactive sources.

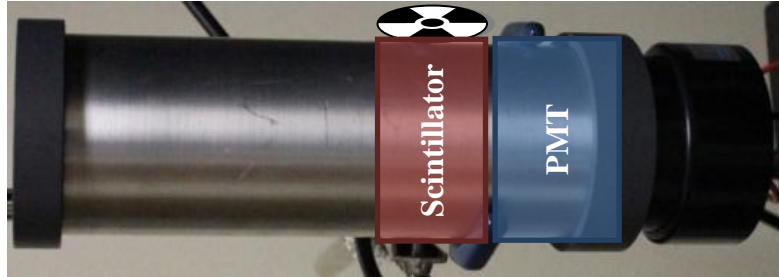


Figure 4.3: Photo and schematic of  $\gamma$  scintillation test station.

The aluminum cylinder houses the scintillator material and the PMT, protecting both from stray light. Radioactive sources are placed at the sides of the cylinder to maximize detector coverage. At right is the electronics housing which supplies voltage to the PMT and delivers the output signal to the ADC

For our measurements, the sources were placed at the sides of a light-tight enclosure containing the test scintillator and a photomultiplier tube. As gamma rays exit the  $^{60}\text{Co}$  or  $^{137}\text{Cs}$ , they pass almost unhindered through the aluminum walls of the enclosure and deposit their energy in the scintillator material. Secondary photons emitted by the nanoparticles or crystal enter the PMT, and an electrical signal is generated and passed to the downstream electronics. Here, an amplifier increases the signal height and an analog-to-digital converter (ADC) processes the shaped pulse from the PMT into a bin based on integrated charge; a higher charge, or greater time-voltage product, indicates a more energetic incident photon. The value from the ADC is passed to a computer running the MAESTRO nuclear physics software suite. This program maintains a running tally of the counts for each bin and develops, over time, a graph of the gamma spectroscopy result from the radionuclide.

Each radio source produces a characteristic pattern of photopeaks generated not by Compton scattering in the scintillator, but by the full deposition of the  $\gamma$  ray energy; the positions of these peaks may be used to identify the source after calibration and further analysis. By using the  $^{137}\text{Cs}$  and  $^{60}\text{Co}$  sources simultaneously, a spectrum with three peaks is produced, and the data is output to Excel for fitting. Regression analysis is used to correlate the positions of the three peaks to the known values for the particular sources, and that fit is extended to the remainder of the bins. Through this process, we may translate the bin-value output from the ADC to the more relevant—and voltage-independent—energy spectrum. Additionally, these peaks are then used to determine the energy resolution of the detector material at a particular photon energy level, with a simple calculation: the ratio of the full-width at half-maximum (FWHM) in keV divided by the centroid peak value. Proper selection of PMT voltage and gain measurements allows for maximum precision at a desired energy level for a particular scintillator; settings used for each scintillator under test are given in the corresponding sections below. Changing the voltage and gain factors, even when using the same scintillator material, affects the positioning of the x-ray backscatter peak(s), Compton edge, and photopeaks, and the conversion equation and energy resolutions should be recalculated whenever the electronics settings are altered. This introduces some uncertainty into comparative measurements of different scintillators, but this is minimized by using the same sources for each measurement and positioning the measured photopeaks at the same bin region each time.

#### *4.1.4 X-ray Diffraction*

The powder XRD technique is especially useful for examining the crystal structure of inorganic nanoparticles, or any type of particle which exhibits a tendency to crystallize. A small sample of the material to test is mounted on a copper grid in a goniometer, then bombarded with x-rays from a carefully calibrated source; for the Bruker system used to evaluate our samples, it is 1.5406 Å, using a source current of 30 mA and accelerator voltage of 40 kV. As the x-rays scatter elastically through the material, they generate a characteristic pattern of bright and dark interference fringes measured by a photodetector which moves around the sample. By measuring one set of reflections, then rotating the sample and repeating the measurement, the system can produce a three-dimensional model of the internal structure of a crystal, or the elemental composition and phase distribution of a nanoparticle sample. Many well-studied compounds are included in a catalog compiled by the Joint Committee on Powder Diffraction Standards (JCPDS), which allows quick determination of crystal formation without a full structural solution.

The XRD spectra are presented as a measure of reflected intensity at a particular scattering angle; sharper peaks indicate better crystallization, though it is possible to have multiple, overlaid responses from different crystal phases. For our particles, with a desired size under 150 nm in diameter, the patterns contain a significant amount of noise, typically due to size dispersion and non-homogenous composition within the particles themselves. Even so, XRD results may confirm the phase purity of a nanocrystal—for instance, YAM, YAP, or YAG for the yttria-alumina family—or ensure that some dopant is fully included in the crystal structure and not simply adsorbed onto the surface. For very small NPs, particles with particular morphology (core-shell structures, amorphous products, etc.), or those which require a solution environment, TEM and SEM are more useful for structural studies, though XRD may still provide information on elemental composition.

#### *4.2 Synthesized Material Analysis*

Results for each of the materials under consideration appear below, accompanied by a discussion of their performance. Except for the commercial NaI scintillator, each NP type tested was produced in our lab specifically for purposes of evaluating its suitability for radiation detection applications. Chapter 5 will present the final evaluation of the various products.

#### 4.2.1 Sodium Iodide (Thallium Activated)

As expected, NaI(Tl) showed the highest  $\gamma$ -ray response and a clear photopeak for both  $\gamma$  sources of all the materials used in this study. Since this crystal is known for its excellent scintillation properties and wide commercial use, we retained its test results as a goal and comparison point for the experimental nanoparticles. When NaI(Tl) was installed in our gamma response setup, we adjusted the electronics settings in order to produce an appropriate scaling and sensitivity based on typical gamma-spectroscopy guidelines. We achieved a representative result with a PMT high voltage (HV) of 900V and a gain factor of 2.330. With these settings, we developed the data shown in Figure 3.2 and Figure 3.3; the three photopeaks, two from  $^{60}\text{Co}$  and one from  $^{137}\text{Ce}$ , are clearly visible. This data was passed to Excel and processed with a linear regression to convert bin number to energy level. The resulting conversion equation is  $E = -41.5393 + 2.7664 \cdot b$  where  $E$  is the photon energy level and  $b$  is the bin number recorded in the raw data; based on the known peak values, we calculate the  $R^2$  data-fit agreement value to be above 99.99%. Using the calculation from 4.1.3, the energy resolutions are then 8.369%, 7.059%, and 6.653% (in ascending energy), and the average resolution over this range is 7.360%.

In the cabinet XL system under the conditions used for NP testing, the NaI(Tl) crystal produces 142,858 cps. While this figure is indeed quite high compared to the ~65,000 cps produced by YAG powder under similar conditions, it must be considered that the NaI is a solid, transparent crystal, while much of the internal YAG luminescence is scattered before reaching the surface of the material. In our conclusions, we examine the possibility of YAG compression to increase transparency and align grain boundaries while maintaining the easier and faster nanoparticle synthesis route.

#### 4.2.2 Lanthanum Fluoride

$\text{LaF}_3$  doped with cerium and terbium in various levels was first evaluated through photoluminescence performance, and selected dopant combinations prepared by solid-state diffusion are shown in Figure 4.4. Of special note in the figure are the spectra for 90-10-0 (La-Ce-Tb) and 90-9-1. Although the doping ratio for  $\text{Ce}^{3+}$  ions only differs by 1%, the intensity of the characteristic  $\text{Ce}^{3+}$  emission around 285 nm is greatly decreased in the latter. At the same time, the intensity of the typical  $\text{Te}^{3+}$  4-peak system at 488 (obscured by reflection), 540, 582, and 620 nm is strongly increased. Together these peak

height changes indicate energy transfer from Ce to Tb ions. Transfer is also seen in the 99-1-0 and 90-1-9 samples; the intensity of the 285 nm peak decreases to about one-fifth its original height while the 540 nm peak increases off scale from an initial level indistinguishable from the broad 285 nm doubled reflection. Numeric integration of the ranges from 270–350 nm and 525–650 nm for both of these traces results in values of ~28,507 for the 99-1-0 iteration and ~29,474 for 90-1-9; although the total luminescence increase is only about 3%, the amount of light generated in the longer-wavelength region is doubled. The lowest-energy peak, around 620 nm, does not have sufficient energy to consistently overcome the photocathode work function in a typical PMT, but the intensity of the other two  $\text{Tb}^{3+}$  peaks supports the use of this scintillator with many existing radiation-detection installations.

Further support for  $\text{LaF}_3$  as an appropriate scintillating material comes from a study of its emissions under x-ray excitation. In our setup, we are not able to measure the UV range, due to limitations of the spectrometer's beam separation system. However, we are able to take precise measurements of the

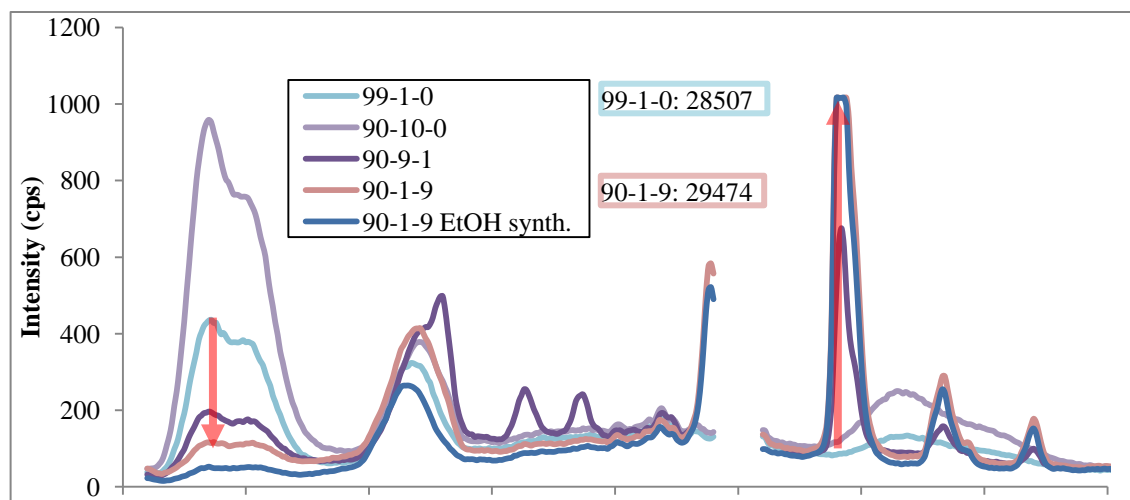


Figure 4.4: Selected PL spectra of  $\text{LaF}_3\text{:Ce,Tb}$ .

These samples were prepared by SSD, except for the trace identified as wet synthesis. Labels given are molar doping percentages of lanthanum (host), cerium, and terbium, respectively. The gap at ~500 nm is due to a first-order reflection peak from the 250 nm excitation source. Red arrows show the decrease in  $\text{Ce}^{3+}$  emission with increase of  $\text{Tb}^{3+}$  peaks with the same Ce concentration, indicating energy transfer, and the inset shows the integrated luminosity across the UV-vis range.

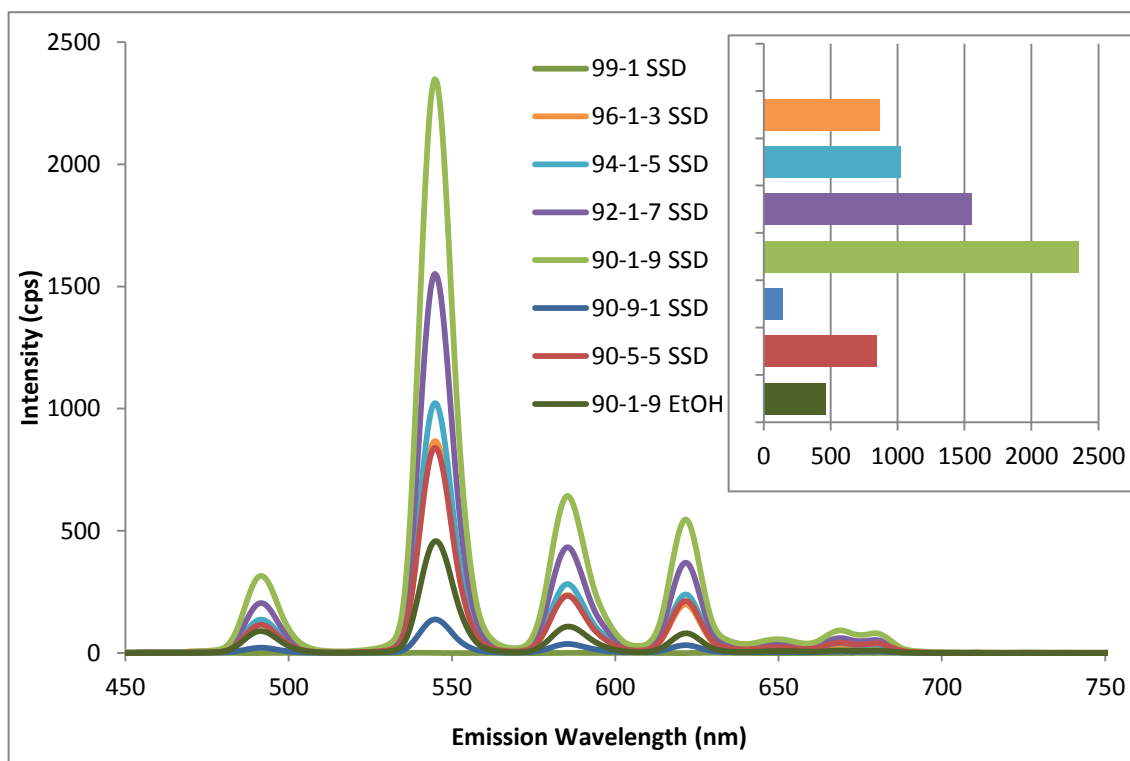


Figure 4.5: Selected XL spectra of  $\text{LaF}_3\text{:Ce,Tb}$ .

These samples were prepared by SSD, except for the trace identified as EtOH wet synthesis. The inset chart shows the greatest peak height between 500 and 700 nm for comparison of emission intensities.

$\text{Tb}^{3+}$  emissions, which demonstrate an excellent response, shown in Figure 4.5. The sample with no terbium doping shows no x-ray response, since all Ce scintillation emissions are in the UV range; as previously discussed, without an energy transfer system or wavelength-shifting dye, Ce doping alone is unsuitable for PMTs without special photocathodes which allow UV detection. The wet-synthesis product demonstrates similar PL response to its SSD counterpart (with the same doping ratio), but the XL performance is significantly increased. Also in Figure 4.5, we compare the maximum intensity of several samples of identical composition at different stages of production: completed SSD-synthesis powder, wet-synthesis (EtOH as solvent) as a freshly-prepared paste, and the final, air-dried powder product of the EtOH method. It is evident that the wet-synthesis method has produced a sample with greatly intensified XL emissions; the mid-grade emission level from the undried sample is consistent with measurements of other NPs which show a quenching effect when using liquid solvents for XL measurements.

Though the emission intensity for the Ce/Tb co-doped particles is quite high, these were prepared without surface modification; adding them into a standard PVT solution gives estimated loading levels of <1% by weight, and the transparency of the resulting polymer is very low. There are some preparation methods that might improve the suspension properties; one option is to include a small amount of oleic acid (structurally,  $\text{CH}_3(\text{CH}_2)_7\text{CH}=\text{CH}(\text{CH}_2)_7\text{COOH}$ ) in the wet-synthesis procedure[8]. Figure 4.6 shows the tail of the x-ray scintillation of  $\text{LaF}_3\text{:Ce}$  prepared through this method. To further increase the measurable scintillation response, we could include PPO and/or POPOP in the toluene solution and subsequent polymer; the dyes, toluene, and the PVT monomer all have benzene-derivative structures and are mutually soluble. Other research has shown that implementing this sort of energy chain increases luminescence decay lifetime, but may increase total luminescence output in the suitable range for the PMT. Using  $\text{Tb}^{3+}$  doping to shift the wavelength is also a possibility. However, the decay lifetime for  $\text{Tb}^{3+}$  is approximately 3 ms, depending on preparation method, particle size, and dopant concentration; this value is several orders of magnitude longer than the  $\sim 1\text{ ns}$  desirable for high energy resolution spectroscopy measurements[23].

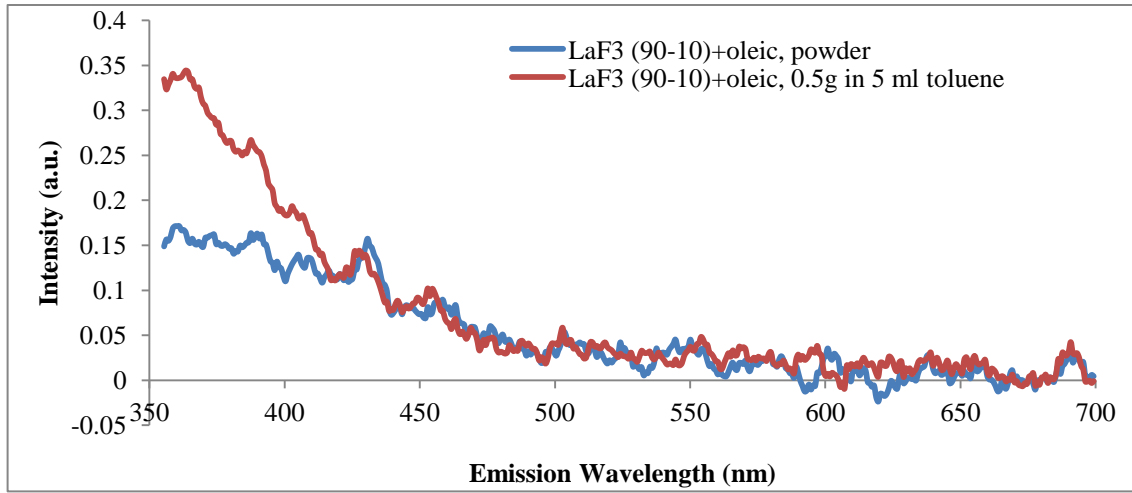


Figure 4.6: XL emissions of  $\text{LaF}_3\text{:Ce}$  prepared through EtOH / oleic acid wet synthesis.

Some emission is seen in the short-wavelength section, and although solution samples usually exhibit a quenching effect, the toluene suspension produces notable emission by wavelength shifting into the detector's range of sensitivity.

#### 4.2.3 Yttrium Aluminum Garnet

YAG:Ce also showed a strong response to both PL and XL testing. These samples were mostly prepared by the modified glycothermal method, using Al-isopropoxide as the aluminum source and a mixture of PEG-200, 1,4-BG, and isopropanol as organic solvents. Other methods used are noted in the appropriate figures, where such data was relevant for comparison.

To confirm crystallization of the products, we submitted a selection of YAG:Ce samples of varying doping ratios for XRD analysis. The results, in Figure 4.7, clearly show formation of single-phase YAG; there is a characteristic (420) peak at  $2\theta \approx 33^\circ$ , and the other visible peaks align with the standard reference from JCPDS No. 33-0040. Some noise is expected, since the nanoparticles are not formed as a single crystal. As seen in the PL and XL traces of YAG:Ce 99-01 in Figure 4.8, the intense x-ray emission from this compound is quite high. Compared to the NaI(Tl) commercial scintillator (in section 3.4), our best-performing YAG:Ce NPs (99-01 by MGM) possess about 46% of the single-crystal luminosity. The remaining issue that would prevent industrial adoption of YAG:Ce as a scintillator lies in its powder form. Several options exist for circumventing this. As mentioned in section 2.1.5, work has been done to compress YAG nanopowders into single-unit ceramics, with a high degree of transparency. Our samples produced through the modified glycothermal method use the same composition and MgO dopant, so a next step would be to design a reusable compression system to test this route. We have also developed a collaboration through the Department of Engineering to explore using a glass slide embedded with nanoparticles; a diffusion process at relatively low temperatures ( $\sim 600^\circ\text{C}$ ; compare with the YAG synthesis point of  $1100^\circ\text{C}$ ) allows the particles to move into the glass.

We also tested a combination of YAG:Ce,Yb at 90-5-5%. Under XL analysis, the ytterbium dopant emits a complex series of peaks in the NIR range, specifically 900–1000 nm (Figure 4.9). These wavelengths are invisible to the human eye and lower than the sensitivity range of most PMTs, though still suitable for Si-based CCDs or InGaAs semiconductor detectors. Noting that the  $\text{Ce}^{3+}$  XL does not decrease with the addition of  $\text{Yb}^{3+}$  as a co-dopant, it is unlikely that we have any energy transfer. Additionally, the slow Yb emission, like Eu and Tb, is unsuitable for radiation detection purposes. However, tagging of materials with NPs of this type would permit invisible identification of personnel or materiel by excitation



with a source at  $\sim 940$  nm. Such a system could be used as an NIR tracking dye, or to facilitate identification in low-light environments where infrared-vision apparatus is already in place.

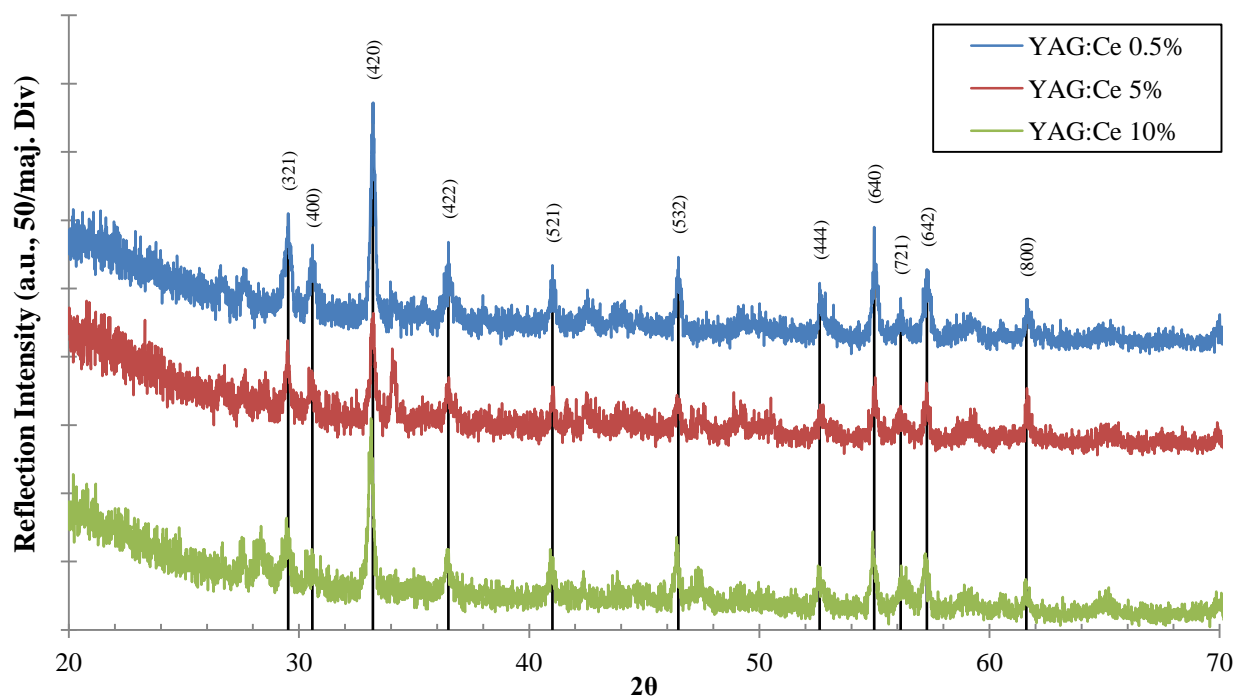


Figure 4.7: XRD analysis of YAG:Ce nanoparticles.

Vertical and horizontal scale is identical for the three traces, but the data have been vertically shifted to clearly show peak alignments. Samples were produced with modified glycothermal method. Key reflection points are marked and closely match JCPDS card 33-0040 for YAG.

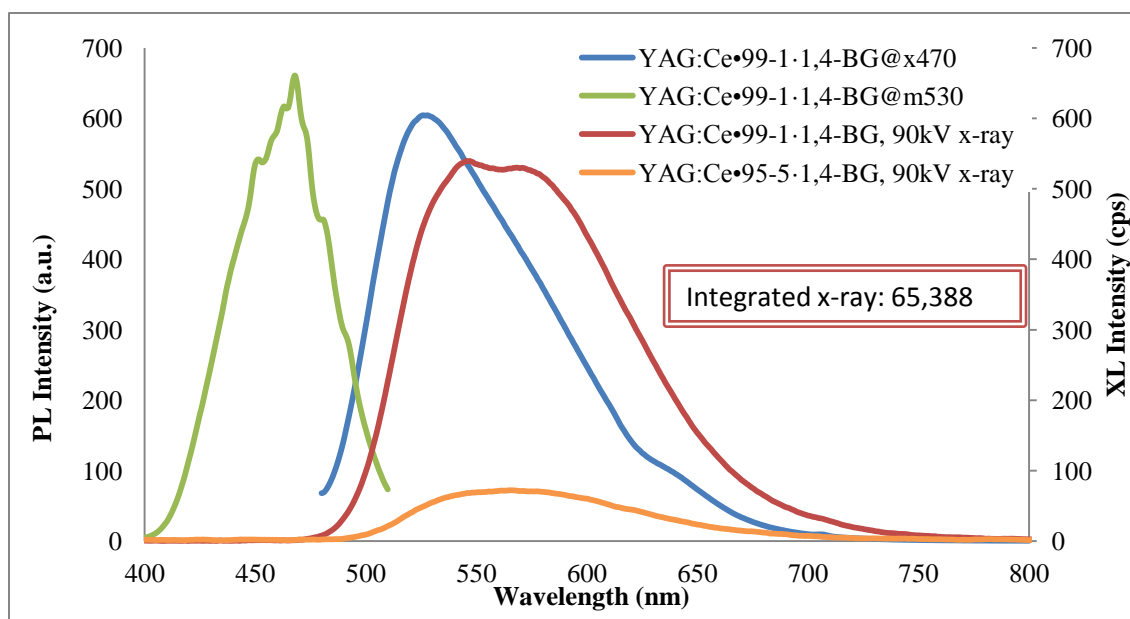


Figure 4.8: PL and XL results of YAG:Ce samples.

Produced through the modified glycothermal method, showing clear response from visible and x-ray excitation. Inset is the integrated XL area for comparison with NaI(Tl).

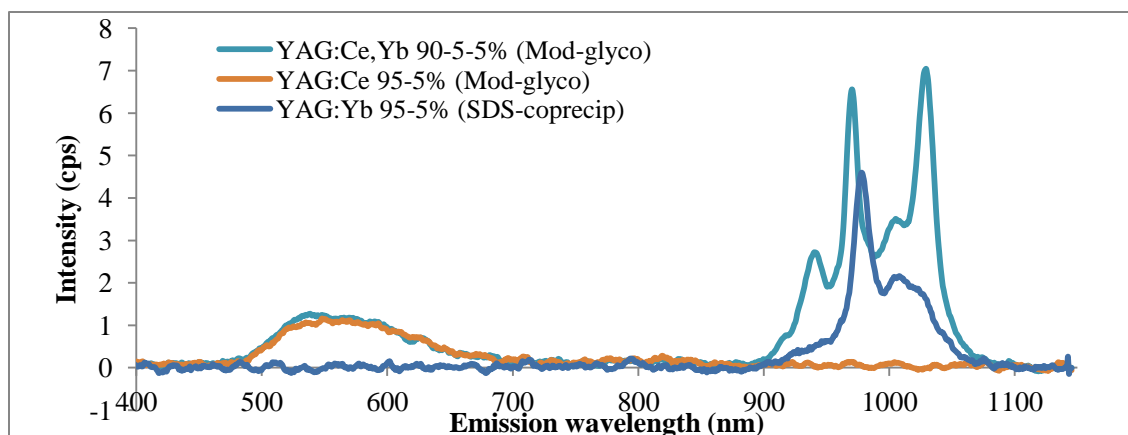


Figure 4.9: XL emissions of YAG:Ce,Yb samples.

NIR emissions are clearly visible, though no energy transfer is apparent. The sample produced through the SDS method, rather than the modified glycothermal technique shows a different peak structure due to alternate oxygenation state populations.

#### 4.2.4 Strontium Fluoride

Extending previous work with rare earth doped  $\text{MgF}_2$  and  $\text{CaF}_2$ , we found  $\text{SrF}_2$  to also exhibit strong PL and XL, with significant  $\gamma$  scintillation over background, even in small quantities. Figure 4.10 compares the PL between our representative  $\text{SrF}_2$  samples and  $\text{CaF}_2$ , each doped with  $\text{Mn}^{2+}$  (0.1 mol%) and  $\text{Eu}^{2+}$  (0.085 mol%) and prepared as shown in Table 3.1. This figure also presents a comparison of  $\text{SrF}_2$  prepared by pure SSD and the highest-output iteration developed through the co-precipitation/suspension

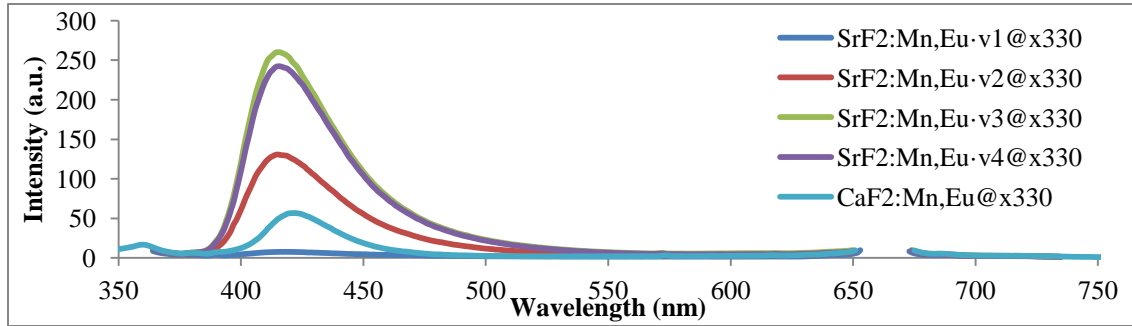


Figure 4.10: PL response of  $\text{CaF}_2$  and  $\text{SrF}_2$  produced through various conditions.

The sample mixed in EtOH solution and sintered for 4 hours (v3) exhibited the highest peak intensity.

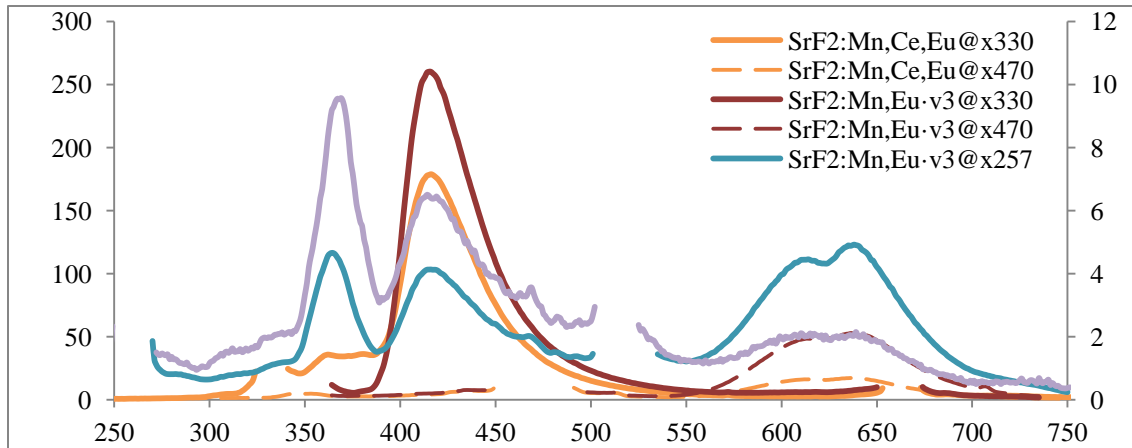


Figure 4.11: Two-peak emission from  $\text{SrF}_2\text{:Mn,Eu}$

The different Eu ionic species produce peaks at corresponding short (2+) and long (3+) wavelength regions. Typically, they require two separate wavelengths to express both sets, but by using 257 nm excitation, both groups are visible at once, albeit with reduced intensity. The peak at  $\sim 360$  nm in the blue and purple traces is due to an instrumental effect, and was discarded when considering comparative performance.

synthesis implemented for later samples. The PL response is greatly increased in the higher-dispersion wet method because it allows better distribution of the small quantity of dopants.

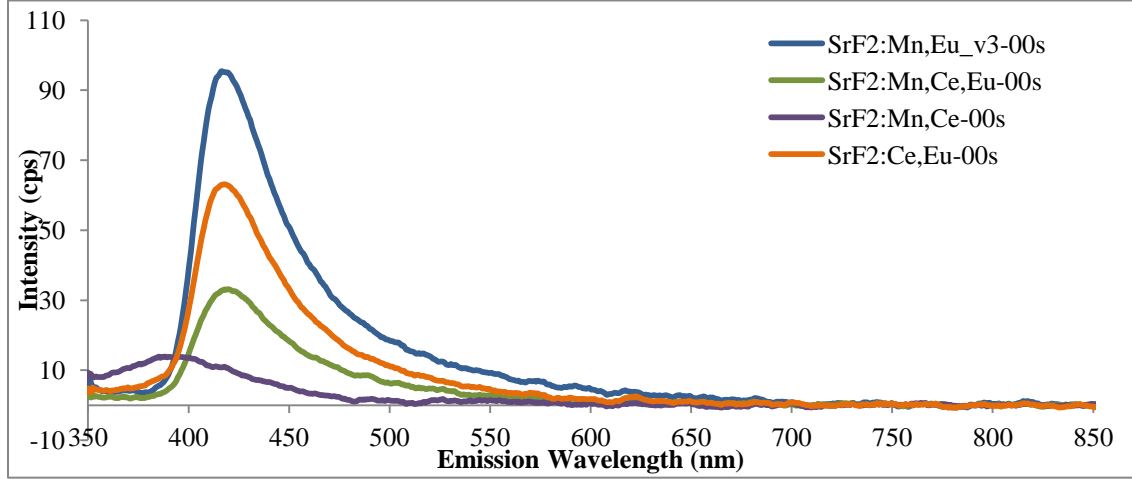


Figure 4.12: Initial x-ray response from  $\text{SrF}_2$  samples.

With no previous exposure to x- or  $\gamma$ -radiation, only  $\text{Eu}^{2+}$  is visible in the XL spectra.

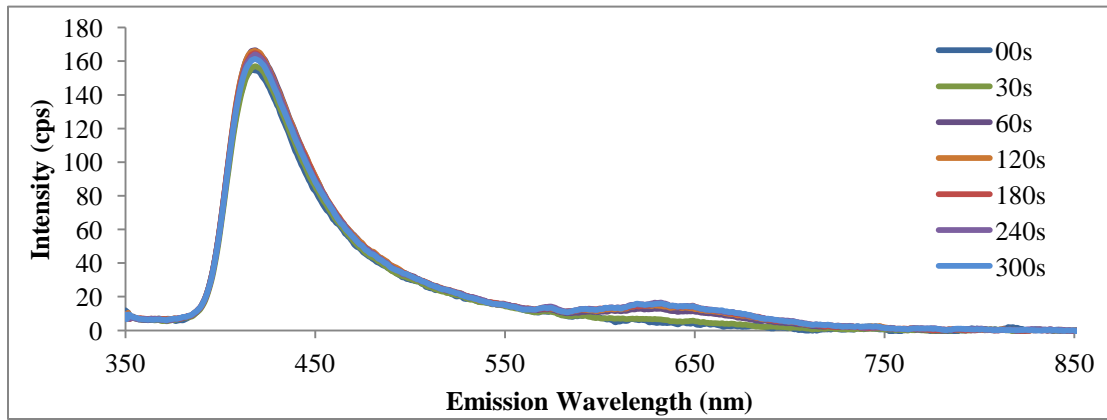


Figure 4.13: 90 kV x-ray response over time in  $\text{SrF}_2\text{:Mn,Eu}\cdot\text{v3}$ .

No significant change is seen, though some structure appears inconsistently at 650 nm; these peaks are not a clear indicator of FIR-type peak shifting.

Though the PL data revealed strong emission peaks were located in the shorter-wavelength end of the PMT's sensitive range, our primary aim with  $\text{SrF}_2$  was to consider its applicability in fluorescence intensity ratio testing. As described previously in section 3.3, we consider two emission peaks from the

sample and consider the changes in these peak heights with increasing radiation dosage. During preparation for the experiment, we determined that the most cost-effective detector assembly for using this technique would employ only a single test-excitation wavelength to produce both peaks for the FIR comparison; in view of that design goal, the sample was tested across a broad range of wavelengths to select a suitable excitation point at 257 nm (see Figure 4.11). Though this is well into the UV range, this particular position holds a few advantages given the FIR detector setup. First, the two peaks for FIR are approximately the same height, reducing the measurement effects of any noise plateau or nonlinear intensity response. Additionally, excitation at this wavelength would have reduced effect on the PMT for scintillation detection, if such a system were included in a dual-purpose detector. Specifically, the detector would consist of a section of scintillating material with data collected through a standard PMT (most sensitive in the visible range), and the second portion would operate on the FIR technique, with light collected from the radiation-damaged material with a dual-wavelength photospectrometer (tuned to the resulting peaks from 257 nm excitation).

SrF<sub>2</sub> has significant x-ray scintillation, seen in Figure 4.12, but only one species, Eu<sup>2+</sup> emits visibly over background; the Eu<sup>3+</sup> and Mn<sup>2+</sup> structures seen in the PL data are covered by the tail of the larger peak. However, x-ray damage may disrupt the stability of Eu<sup>2+</sup> and force its conversion to the higher oxidation state, visible as a drop in the short-wavelength peak and a shoulder at longer wavelengths. Using a small quantity of the highest-output, synthesis-optimized sample from initial testing, designated as SrF<sub>2</sub>:Mn,Eu·v3, we instituted a process of x-ray exposure and PL measurements. The results of this testing are shown in Figure 4.13 and Figure 4.14. The first figure was performed with exposure to 90 kV x-ray, but the intensity of this beam is ~10<sup>6</sup> times that of a typical  $\gamma$ -emission source used for testing. Additionally, the higher energy x-radiation has a lower cross section, even with SrF<sub>2</sub>'s increased effective Z over MgF<sub>2</sub> or CaF<sub>2</sub>. We saw insufficient evidence for FIR changes over short-term exposure at the higher x-ray energy, as shown in Figure 4.13. For a second round of testing, we replaced the powder with an unexposed portion of the v3 sample and employed a lower x-ray energy (50 kV). Care was taken to ensure consistency in measurements during and after each exposure and PL measurement. Maxima for the largest Eu<sup>2+</sup> and Eu<sup>3+</sup> were identified and compared, and the areas under each peak were also determined through

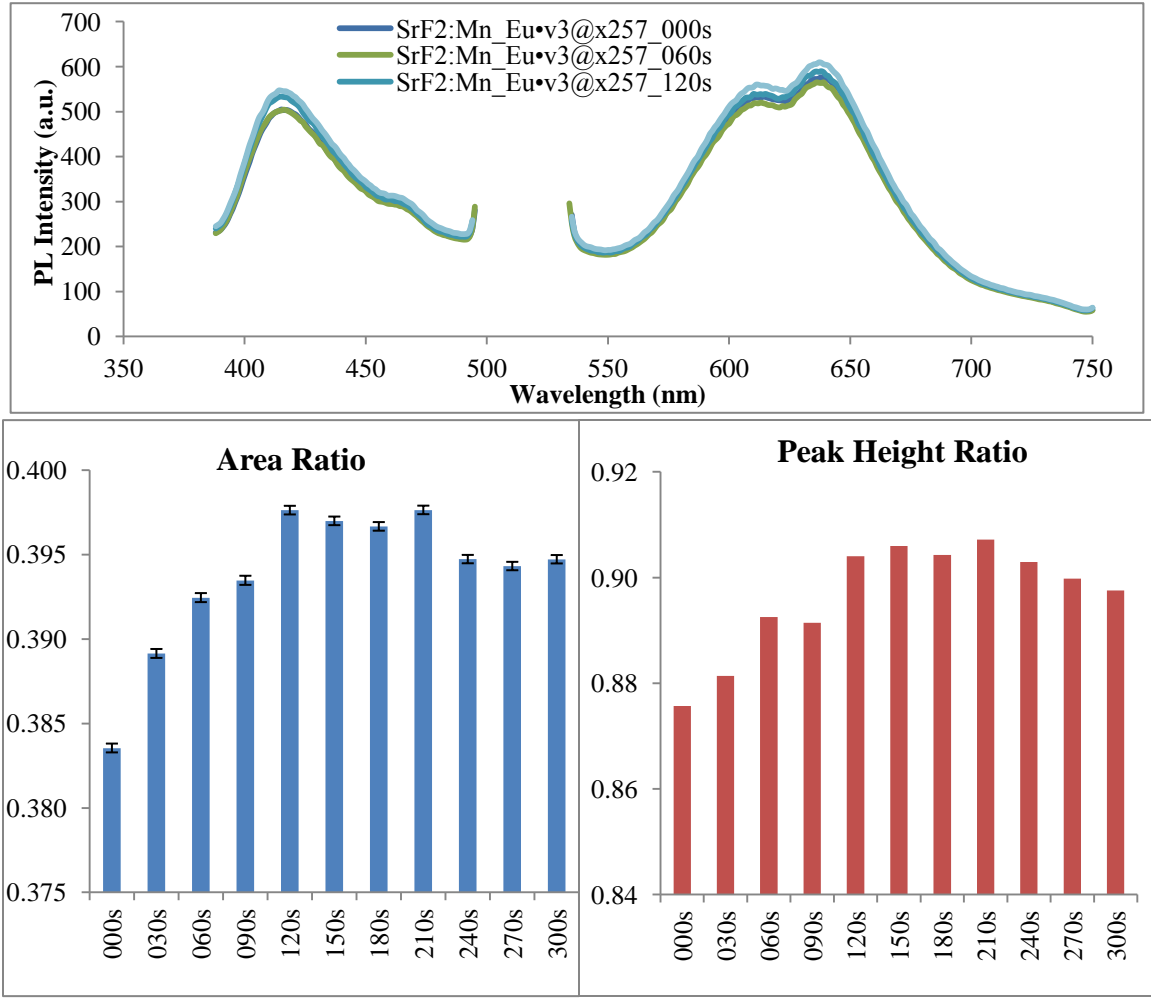


Figure 4.14: 50 kV x-ray testing of SrF<sub>2</sub>:Mn,Eu.

The top figure shows the changes in PL intensity with increasing x-ray dose. The bottom sections quantify the ratio of the short and long wavelength (Eu<sup>2+</sup> and Eu<sup>3+</sup>) integrated areas and peak heights to search for FIR-quality height changes.

$$Area = \left[ \frac{(b_1 + b_n)}{2} + (b_{n-1} - b_2) \right] * h$$

a modification of the trapezoid method for numerical integration. The lower exposure does seem to allow for some structure in the data, as seen in Figure 4.14, but there is still no clear trend. Several factors may affect the physical properties of the crystal that lead to this observation. First, the higher effective Z of the SrF<sub>2</sub> sample over the other group-2 elements may increase the cross section to the point where x-ray

exposure with this type of cabinet system is too intense; if the detector is sensitive to very low intensity emissions from a radiological gamma source, the small FIR effect generated by that exposure would be equivalent to a fraction of a second in the x-ray cabinet. This possibility led to the design and construction of a new FIR detection system, described in section 5.2. The second is that the larger electronic shells in  $\text{Sr}^{2+}$  might allow recombination through the valence and conduction bands, effectively self-correcting for some radiation damage by ensuring that Eu ions in the host may reduce back to  $\text{Eu}^{2+}$ .

Despite weak results from X-ray-induced FIR testing,  $\text{SrF}_2$  does also show a strong response in standard scintillation tests. In Figure 4.15, the optimized v3 sample produces a huge number of counts for a  $\gamma$  source ( $^{137}\text{Cs}$ ) and a noticeable signal for a  $\beta$  source ( $^{22}\text{Na}$ ); using the same electronics settings, the control situations did not register significant activity. Without sources present, with radioactive sources but no scintillator, or with only the PMT, less than 2000 events are noted. However, the  $\beta$  source produces ~39,000 counts and the  $\gamma$  source elicits over 900,000. No photopeaks are visible, but the sample produced was very thin, on the order of 1 mm, so the incoming particles did not pass through sufficient radiation lengths to deposit all their energy. A thicker series is under production, based on the results of this testing. Even if  $\text{SrF}_2$  does not prove to be an effective material for FIR-type detectors, it may have a place as a normal scintillating material based on these results.

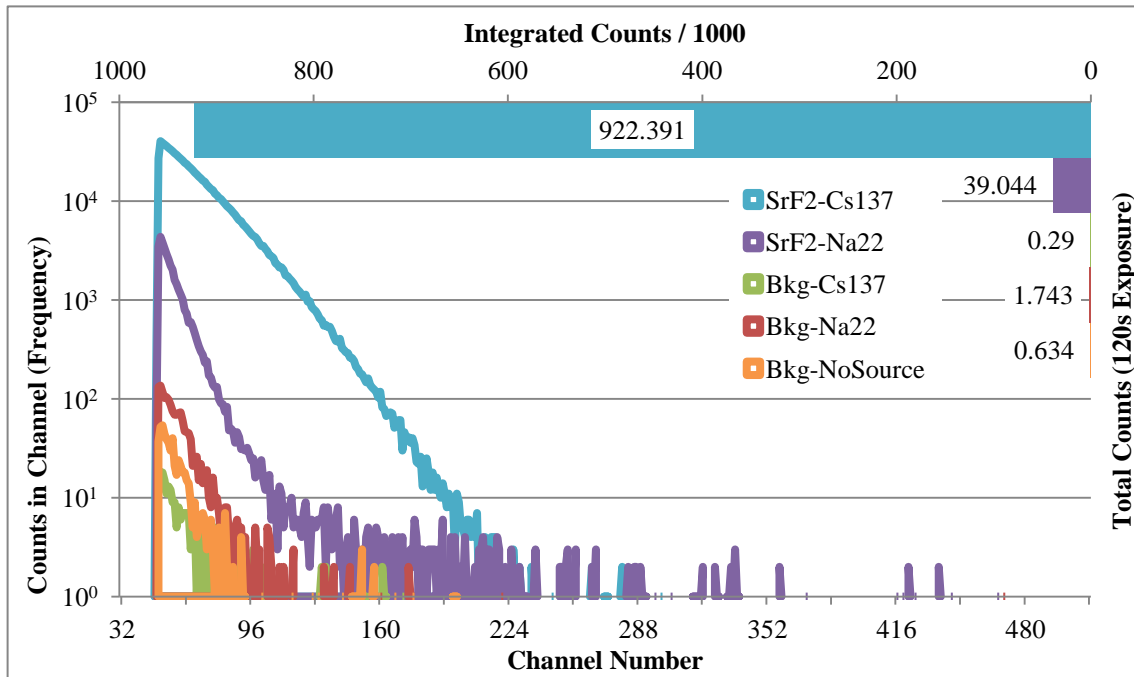


Figure 4.15: SrF<sub>2</sub>:Mn,Eu gamma scintillation response.

The upper bar chart shows total integrated counts for the sample (10 mm x 10 mm x 1 mm) for both experimental and control configurations, demonstrating notable response for  $\beta$  ( $^{22}\text{Na}$ ) and  $\gamma$  ( $^{137}\text{Cs}$ ) sources. Traces in the lower portion show channel distribution of counts; no photopeaks are visible, but some discrimination is possible between source particle types.



## Chapter 5

### Conclusions and Extension to Future Research

Nanomaterials, once in the realm of science fiction, have experienced an explosion of development, evincing new syntheses and applications with each passing month. Seeking improvements over existing detector assemblies, and endeavoring to explore the possibilities for lower-cost, high-sensitivity installations that could be produced for any system that must cope with large cargo or personnel flux, our group has proposed several nanoparticle alternatives to traditional materials. Many of these are the <100 nm diameter analogs of bulk scintillating compounds, like YAG:Ce. Others, like ZnO, do not show luminescence except at the small scales where quantum confinement effects begin to dominate. Many groups have pushed the envelope for nanoparticle capabilities, with various measures of success. For nanoscintillators specifically, the verdict is still out on the feasibility of replacing existing materials, but the auspicious results we have observed certainly do not rule out the superiority of nano-solutions for our target application of radiation detection, and our group's related work in nanomedicine treatments.

#### 5.1 Evaluation of Nanoparticle Performance

By preparing and characterizing a variety of nanoparticle candidates for radiation detection, we were able to evaluate their suitability for that and related applications. LaF<sub>3</sub>, doped with Ce<sup>3+</sup> and Tb<sup>3+</sup> had previously been considered by our group, though those samples were produced through a different process. Our new testing of doped LaF<sub>3</sub> shows strong PL and XL response, with multi-peak emissions in the near-UV and visible-green regions. However, the visible emission, where existing PMTs are highly sensitive, is due to a long-lived Tb<sup>3+</sup> emission; this phosphorescence, with a lifetime on the order of milliseconds, is orders of magnitude slower than the desired timing of <50 ns appropriate for scintillation detectors. Our testing also shows significantly brighter x-ray luminescence emissions from samples prepared through the solid-state diffusion method than from those produced by wet chemistry. This situation necessitates a choice between bright luminescence or mid-synthesis surface modification. The high temperatures required for SSD would vaporize any organic solvent, so modification would have to be done post-sintering. For ethanol-solution preparations, further study is necessary to determine the optimal conditions to improve

luminescence. It may also be possible to use oleic acid, 1,4-butylene glycol, or other high-boiling-point organic solvents to allow crystallization while maintaining toluene-compatible surface groups. However, it may be more prudent to move on from  $\text{LaF}_3$  altogether and investigate other materials which we found to have better characteristics for scintillation detection.

The exploration of  $\text{YAG:Ce}^{3+}$  provided just such an opportunity. While the easiest synthesis is still the SSD method, there are also combination sintering and organic methods, specifically the modified glycothermal method, which do not require the expensive iridium crucibles or pressure-controlled reaction vessels of some other methods. Compared to results in literature, the PL and XL response is somewhat lower in our product than is reported for those produced through the specialized methods, but the lower start-up costs and easy scalability of the simpler procedure may overcome that difficulty for wider applications.  $\text{YAG:Ce}$  has a broad, bright emission centered at 530 nm, well within the target range for PMT matching. This also places it near the emission of existing commercial  $\text{CsI(Tl)}$  crystals, leading to easier upgrade or replacement of current systems. The XL response is red-shifted slightly, likely due to a new relaxation route opened by the scintillation process. Removing inner shell electrons with  $\gamma$ - or x-radiation permits alternate channels for outer shell electrons (with appropriate restrictions on spin state, momentum, and angular momentum) to cascade inwards, leaving behind valence holes that are not typically exposed through PL excitation. The shifted wavelength is not sufficiently changed so as to degrade PMT matching or response.  $\text{YAG:Ce}$  is also a candidate for a new round of post-synthesis processing, by compressing the material into a solid ceramic disk or embedding the particles into glass. The first procedure does not technically result in a nanoparticle product, but the preparation does not require a pure crystal and the final disk maintains the transparency necessary for good optical photon emission other advantages of a single-crystal detector without the necessity of growing a pure, monolithic unit. Glass doping is also an interesting option for high-temperature synthesis materials; stability at this point allows diffusion techniques or custom molten-glass compositions which also provide one material with matched refractive indices, high mechanical stability, and, again, no need for growing a single crystal.

$\text{SrF}_2$  remains a promising material for detection research. Early studies of similar group-2-rare-earth compounds demonstrated the FIR response necessary for hypersensitive radiation detection.

However, our testing with the higher-Z compound did not show a significant change of this nature. Despite this, the synthesis of  $\text{SrF}_2$  is simple and easily scalable, and PL and XL stimulation revealed strong peaks which may be employed for standard gamma or beta particle detection. The visible emission maxima are in the shorter range of PMT sensitivity when using 330 nm excitation, and those produced under 470 nm are far towards the orange and red region, and are more suitable for use with a photodiode with high quantum efficiency in that longer wavelength range. The significant  $\gamma$ -ray count production also indicates that  $\text{SrF}_2\text{:Mn,Eu}$  could be used as a traditional scintillator.

## 5.2 Project Extension

Through our collaboration with the College of Engineering, we have been able to greatly expand our testing abilities. The Radiation Measurement Application Laboratory has been an invaluable part of our efforts to characterize  $\beta$  and  $\gamma$  response of nanoparticles with real detector technologies coupled with experienced personnel. Our next phase of work includes a new association with Industrial Engineering. The team's work with glass microfluidics and micro-scale machining techniques will allow a new series of tests on suitable particles.  $\text{YAG:Ce}$ , produced in the experiments recorded here, is stable at high temperatures and will not evolve dangerous gases like  $\text{SrF}_2$ . Various projects undertaken with associated labs have produced other glass, ceramic, and organic-embedded samples, and our characterization efforts have helped to advance research for these other groups as well. Using the refinements and group skills gained from this work, our own group has designed and produced a new assembly that can be used for  $\gamma$  luminescence photospectroscopy and increasing the repeatability of FIR measurements. This device, shown in Figure 5.1, can reduce instrumental effects for appropriate data collection, while allowing easy replacement of the sample under test and the external components that will become part of the prototype field FIR dosimetry system after further refinement.

Nanoparticles remain a field full of possibilities, and with the combined efforts of theorists and modelers, synthesis experts and chemists, and a vast cadre of other experts from diverse fields, the growth of nanoparticle solutions for a wide variety of applications is only the new step in an opening path for human development in the twenty-first century and beyond.



Figure 5.1: FIR and  $\gamma$  luminescence testing assembly.

Clockwise from top: PMT for scintillation measurements; commercial NaI(Tl) crystal (red top); multi-head fiber for delivery and extraction of light; and grey cylinder to maintain light-tightness, protect samples under test and hold radioactive sources in place.

Appendix A  
Apparatus and Instrumentation

Barnstead Thermolyne Muffle Furnace

Operational Temperature Range: 200–1100°C

Ramp-up: Manual control (see individual syntheses)

Bruker Discover 8 Powder X-ray Diffraction System

Anode Type: Copper

Operational Wavelength: 1.5406 Å

Generator Current: 30 mA

Generator Voltage: 40 kV

High Voltage Supply: 774.7 V

Sample raw data output shown below:

CEM Corporation Discover SP with Accuvent

Vial size: 35 ml

Operational Temperature: <300°C

Microwave power: 200 W (maximum applied)

Pressure Limit: 300 psi / 20.68 bar / 2.068 MPa

Faxitron RX-650 Cabinet X-ray System

Target Type: Tungsten

Tube Current: 5 mA

Accelerating voltage: 90 kV

Source-to-target Distance: 30 cm

Output Fiber: 600 µm core diameter, P600-2-UV-Vis (OceanOptics)

OceanOptics QE65000 Spectrometer

Thermo-electric Cooling to -10.00°C

Factory Calibration for Nonlinearity

# Shimadzu RF-5301PC Spectrofluorophotometer

Excitation/Emission Slit Widths: 3.0/3.0 nm or 1.5/1.5 nm, specified for comparison

Excitation/Emission  $\lambda$  Range: 200–900 nm



Figure A.1: Interior and exterior of x-ray irradiation system.

The fiber carries light out to the spectrometer; duration and intensity of irradiation are set using the front panel, which also indicates tube status



Figure A.3: OceanOptics spectrometer.

Input fiber shown connected at bottom right

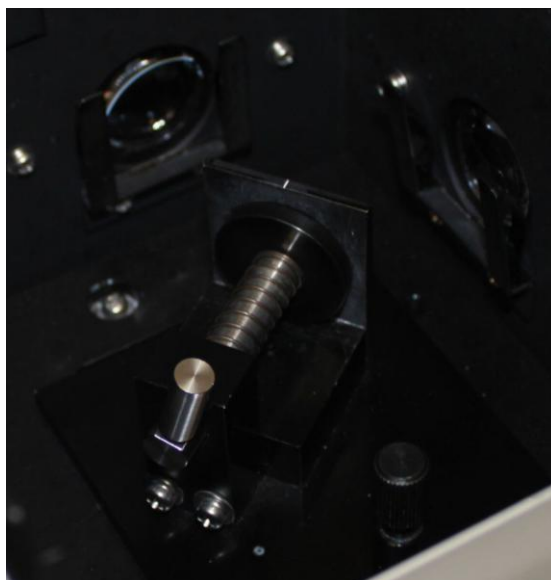


Figure A.2: Interior of Shimadzu spectrofluorophotometer.

Excitation window on right, solid sample holder in center, and emission measurement window on the upper left. Holder may be exchanged for a different assembly for liquid samples



## References

- [1] Safety of Nuclear Reactors, (n.d.).
- [2] C. Miller, A. Cubbage, D. Dorman, J. Grobe, G. Holahan, N. Sanfilippo, Recommendations for Enhancing Reactor Safety in the 21st Century, United States Nuclear Regulatory Commission, 2011.
- [3] S.R. Fahnestock, S.L. Irwin, Synthetic spider dragline silk proteins and their production in *Escherichia coli*, *Applied Microbiology and Biotechnology*, 47 (1997) 23–32.
- [4] M. Zhang, O. Volpert, Y.H. Shi, N. Bouck, Functional Study of Maspin in Breast Cancer, DTIC Document, 2000.
- [5] E.A. McKigney, R.E. Del Sesto, L.G. Jacobsohn, P.A. Santi, R.E. Muenchausen, K.C. Ott, T. Mark McCleskey, B.L. Bennett, J.F. Smith, D. Wayne Cooke, Nanocomposite scintillators for radiation detection and nuclear spectroscopy, *Nuclear Instruments and Methods in Physics Research Section A: Accelerators, Spectrometers, Detectors and Associated Equipment*, 579 (2007) 15–18.
- [6] M. Hossu, Z. Liu, M. Yao, L. Ma, W. Chen, X-ray luminescence of CdTe quantum dots in LaF<sub>3</sub>:Ce/CdTe nanocomposites, *Applied Physics Letters*, 100 (2012) 013109.
- [7] P. Suriamoorthy, X. Zhang, G. Hao, A.G. Joly, S. Singh, M. Hossu, X. Sun, W. Chen, Folic acid-CdTe quantum dot conjugates and their applications for cancer cell targeting, *Cancer Nanotechnology*, 1 (2010) 19–28.
- [8] R.K. Feller, G.M. Purdy, D. Ortiz-Acosta, S. Stange, A. Li, E.A. McKigney, E.I. Esch, R.E. Muenchausen, R. Gilbertson, M. Bacrania, B.L. Bennett, K.C. Ott, L. Brown, C.S. Macomber, B.L. Scott, R.E. Del Sesto, Large-scale synthesis of Ce<sub>x</sub>La<sub>1-x</sub>F<sub>3</sub> nanocomposite scintillator materials, *Journal of Materials Chemistry*, 21 (2011) 5716.
- [9] I. Mukhametzhanov, Z. Wei, R. Heitz, A. Madhukar, Punctuated island growth: An approach to examination and control of quantum dot density, size, and shape evolution, *Applied Physics Letters*, 75 (1999) 85.
- [10] Saint-Gobain Crystals, NaI(Tl) and Polyscint(r) NaI(Tl) Sodium Iodide Scintillation Material, (2012).
- [11] Saint-Gobain Crystals, CsI(Tl), CsI(Na) Cesium Iodide Scintillation Material, (2007).
- [12] E.V.D. van Loef, P. Dorenbos, C.W.E. van Eijk, K. Krämer, H.U. Güdel, High-energy-resolution scintillator: Ce<sup>3+</sup> activated LaBr<sub>3</sub>, *Applied Physics Letters*, 79 (2001) 1573.
- [13] E.V.D. van Loef, P. Dorenbos, C.W.E. van Eijk, K. Krämer, H.U. Güdel, High-energy-resolution scintillator: Ce<sup>3+</sup> activated LaCl<sub>3</sub>, *Applied Physics Letters*, 77 (2000) 1467.
- [14] W. Liu, W. Zhang, J. Li, H. Kou, D. Zhang, Y. Pan, Synthesis of Nd:YAG powders leading to transparent ceramics: The effect of MgO dopant, *Journal of the European Ceramic Society*, 31 (2011) 653–657.
- [15] J. Lu, T. Murai, K. Takaichi, T. Uematsu, K. Misawa, M. Prabhu, J. Xu, K. Ueda, Highly efficient polycrystalline Nd:YAG ceramic lasers, in: *Lasers and Electro-Optics*, 2001.
- [16] H. Geiger, W. Müller, Elektronenählrohr zur Messung schwächster Aktivitäten (Electron counting tube for measurement of the weakest radioactivities), *Die Naturwissenschaften*, 16 (1928) 617–618.
- [17] G.F. Knoll, *Radiation Detection and Measurement*, 3rd ed., John Wiley and sons, 2000.
- [18] M. Deptuch, T.Z. Kowalski, B. Mindur, Selected problems in aging effects with gas proportional counters, *Nuclear Physics B - Proceedings Supplements*, 150 (2006) 394–397.
- [19] High Purity Germanium (HPGe) Detector/Identifiers, (n.d.).
- [20] S.A. Dyer, *Wiley Survey of Instrumentation and Measurement*, John Wiley & Sons, 2004.
- [21] D.L. Andrews, D.S. Bradshaw, Virtual photons, dipole fields and energy transfer: a quantum electrodynamical approach, *European Journal of Physics*, 25 (2004) 845–858.

- [22] W. Moses, S.E. Derenzo, The scintillation properties of cerium-doped lanthanum fluoride, *Nuclear Instruments and Methods in Physics Research Section A: Accelerators, Spectrometers, Detectors and Associated Equipment*, 299 (1990) 51–56.
- [23] J. Wang, S. Bo, L. Song, J. Hu, X. Liu, Z. Zhen, One-step synthesis of highly water-soluble  $\text{LaF}_3\text{:Ln}^{3+}$  nanocrystals in methanol without using any ligands, *Nanotechnology*, 18 (2007) 465606.
- [24] T.G. Barton, R. Guttenberger, H.-J. Foth, Effects of simmer current on flash-lamp impedance and their combined influence on the output of the Ho, Cr, Tm: YAG laser, *Applied Optics*, 34 (1995) 2004–2011.
- [25] S.J. Skinner, J.P. Feist, I.J.E. Brooks, S. Seefeldt, A.L. Heyes, YAG:YSZ composites as potential thermographic phosphors for high temperature sensor applications, *Sensors and Actuators B: Chemical*, 136 (2009) 52–59.
- [26] C.-C. Yang, C.-M. Lin, Y.-J. Chen, Y.-T. Wu, S.-R. Chuang, R.-S. Liu, S.-F. Hu, Highly stable three-band white light from an InGaN-based blue light-emitting diode chip precoated with (oxy)nitride green/red phosphors, *Applied Physics Letters*, 90 (2007) 123503.
- [27] C.W. Won, H.H. Nersisyan, H.I. Won, J.H. Lee, K.H. Lee, Efficient solid-state route for the preparation of spherical YAG:Ce phosphor particles, *Journal of Alloys and Compounds*, 509 (2011) 2621–2626.
- [28] X. Li, W. Wang, Preparation of uniformly dispersed YAG ultrafine powders by co-precipitation method with SDS treatment, *Powder Technology*, 196 (2009) 26–29.
- [29] W. Chen, S.L. Westcott, J. Zhang, Dose dependence of x-ray luminescence from  $\text{CaF}_2\text{:Eu}^{2+}$ ,  $\text{Mn}^{2+}$  phosphors, *Applied Physics Letters*, 91 (2007) 211103.
- [30] W. Chen, S.L. Westcott, S. Wang, Y. Liu, Dose dependent x-ray luminescence in  $\text{MgF}_2\text{:Eu}^{2+}$ ,  $\text{Mn}^{2+}$  phosphors, *Journal of Applied Physics*, 103 (2008) 113103.
- [31] Y. Jin, W. Qin, J. Zhang, Preparation and optical properties of  $\text{SrF}_2\text{:Eu}^{3+}$  nanospheres, *Journal of Fluorine Chemistry*, 129 (2008) 515–518.

### Biographical Information

Ryan had begun to explore the mysteries of the natural world at an early age, developing an interest in both observational and experimental methods. After an exceptional elementary and middle school science experience, with a healthy dose of useless trivia, it was in high school that his desire for knowledge truly blossomed. Biology and chemistry were fascinating in their own way, but physics claimed to be the big adventure, seeking answers to the greatest mysteries, through cosmology, quantum mechanics, and general extension to so many disciplines.

UT Arlington boasted excellent facilities and faculty to continue Ryan's upward trend. As an undergraduate, he joined the fledgling Picosecond Test Facility and worked with many others to produce a new fast-timing detector, which uses Cerenkov light from scattered protons to make timing measurements on the order of 10 ps (enough for light to move almost 3 mm). From his experience there, he moved to the NanoBio Group, seeking to put his detector-design skills to good use to produce new technologies to prevent invasive searches. He still hopes to balance the need for security with the civil rights of the people one seeks to protect.

The future remains full of possibilities for this young man, and there are no bounds on where his work may take him. Research is always fun, but there's the nagging desire to invent a time machine, achieve virtual immortality, or even just manufacture a lost-sock finder that will continue to give him a goal in life, no matter how many times he's chastised for sciencing at things that probably don't need it. Bound by an oath to only use his powers for good, and never for evil, the world should have no fear to meet this newly matriculated scientist as he turns to his next great challenge.